

X-ray Identifications of FIRST Radio Sources in the xBoötes Field

K. EL Boucheffry¹*

¹*Astrophysics and Cosmology Research Unit, University of Kwazulu-Natal, Westville, 4000, South Africa*

Accepted 2009 April 14. Received 2009 April 09; in original form 2008 June 03

ABSTRACT

With the goal of investigating the nature and the environment of the faint radio sources (at mJy level), here are presented results of X-ray identifications of Faint Imaging Radio Survey at Twenty centimetres (FIRST) in the 9 square degrees Boötes field of the NOAO Deep Wide Field Survey (NDWFS), using data from the Chandra XBoötes survey. A total of 92 (10%) FIRST radio sources are identified above the X-ray flux limit f_X (0.5 – 7) keV = 8×10^{-15} erg s⁻¹ cm⁻², and 79 optical counterparts are common to both the radio and X-ray sources. Spectroscopic identifications were available for 22 sources (27%). Multi-wavelength optical/infrared photometric data ($B_w \sim 25.5$ mag, $R \sim 25.8$ mag, $I \sim 25.5$ mag and $K \sim 19.4$ mag) were available for this field and were used to derive photometric redshift for the remaining 57 sources without spectroscopic information. Most of the radio-X-ray matches are optically extended objects in the R band with a photometric redshift distribution peaking at $z \sim 0.7$. Based on the hardness ratio and X-ray luminosity, 37 sources (89%) were classified as AGN-1, 19 as AGN-2, 12 as QSO-1, 2 as QSO-2 and 9 sources as normal galaxies. While the majority of these sources have a hard X-ray luminosity $L_X(2 - 7)$ keV > 10^{42} erg s⁻¹, about one third of the sources have $L_X(2 - 7)$ keV > 10^{44} erg s⁻¹ and therefore classified as QSO-1. The majority (68%) of the radio-X-ray matched population are found to have $\log f_X/f_{opt}$ within 0.0 ± 1 region indicative of AGNs, 23% with high X-ray-to-optical flux ratio ($\log f_X/f_{opt} > 1$), suggesting high redshift and/or dust obscured AGN, and 11% of the radio-X-ray matches that are X-ray faint optically bright sources with $\log f_X/f_{opt} < -1$, and most of these sources are optically extended. These objects are low- z , normal galaxies or low luminosity AGNs (LINERS).

Key words: galaxies: active–galaxies: high-redshift–X-rays: diffuse back ground–X-rays: galaxies

1 INTRODUCTION

X-ray surveys have played a crucial role in our understanding of the nature of the sources that populate the X-ray universe. Early surveys like the Einstein sensitivity survey (Gioia et al. 1990), ROSAT(Roentgen Satellite) International X-ray/optical survey (Ciliegi et al. 1997) and the ASCA (Advanced Satellite for Cosmology and Astrophysics) Large Sky Survey (Akiyama et al. 2000) showed that the vast majority of X-ray sources were AGN. In particular, in shallow wide area surveys in the soft (0.5-2 keV) X-ray band, most of the sources detected are unobscured, broad line AGN, which are characterised by a soft X-ray spectrum with a photon index $\Gamma = 1.9$ (Nandra & Pounds 1994). On the other hand, the number density of AGN identified in the hard X-ray and mid-IR bands is far greater than that found in any optical surveys of comparable depth (e.g. Bauer et al. 2004; Stern et al. 2002a).

A combination of radio data with optical and X-ray photometry provides a considerable wealth of information on the

nature of the faint radio/X-ray population (Stocke et al. 1991). Deep radio survey at 1.4GHz observations consist of two main populations: AGN and star-forming galaxies (Condon 1984; Windhorst et al. 1985). At this frequency the primary emission mechanism in virtually all radio sources is synchrotron emission from relativistic electrons spiralling around the magnetic field within the host galaxy. The radio emission can be related either to ongoing star-forming processes or to the accretion activity onto the central super-massive black hole within the galaxy. At very faint flux densities (μ Jy), studies have shown that the radio population is provided by star forming galaxies, which produce non-thermal radio continuum at 1.4GHz through synchrotron emission from supernovae remnants, while other studies suggested that the radio emission may be caused by ‘radio-quiet’ AGN, rather than star-forming galaxies (e.g. Simpson et al. 2006; Jarvis & Rawlings 2004). At the Jansky and mJy levels, the bulk of the radio source population is dominated by powerful AGNs. Observations of radio emission of AGNs provide clues to the accretion history of the universe and important information in our understanding of how central black holes grow over cosmic time as well as the physical process behind these powerful objects, especially when combined

* E-mail: kelboucheffry@gmail.com

with X-ray observations (e.g. Merloni et al. 2003). They also provide clues to some properties of the interstellar and intergalactic medium.

Previous studies on cross correlations between radio and X-ray surveys have determined a link between the star formation rate and the radio and X-ray luminosities of star forming galaxies (e.g. Condon 1992; Ranalli, Comastri & Setti 2003), which can be combined to determine relationships between radio and X-ray luminosities for star forming galaxies. Bauer et al. (2002) have conducted a study of the faint X-ray and radio sources using a 1 Ms Chandra data set and ultra deep VLA observations, finding a large overlap between faint X-ray and radio sources. These authors have shown that the X-ray and radio luminosities are correlated for nearby late type galaxies, and therefore used it to estimate the star formation rate in their sample. Other studies of the radio-X-ray correlations involve studies of the radio properties of the hard X-ray sources. For example, Barger et al. (2001), cross correlated the VLA data ($S_{1.4\text{ GHz}} = 25 \mu\text{Jy}$), with deep Chandra survey ($f_X(2 - 10 \text{ keV}) = 3.8 \times 10^{-15} \text{ erg s}^{-1} \text{ cm}^{-2}$) finding about 50% radio counterparts to their X-ray sources. Ciliegi et al. (2003), have performed a study of the radio properties of the X-ray sources detected in the HELLAS survey ($S_{5\text{ GHz}} = 0.3 \text{ mJy}$; $f_X(5 - 10 \text{ keV}) = 5 - 4 \times 10^{-14} \text{ erg cm}^{-2} \text{ s}^{-1}$). They find an identification rate of 30% much higher than that of the soft band (0.5-2 keV). At somewhat fainter fluxes ($f_X(2 - 8 \text{ keV}) = 7.7 \times 10^{-15} \text{ erg cm}^{-2} \text{ s}^{-1}$, $S_{1.4\text{ GHz}} = 60 \mu\text{J}$), Georgakakis, et al. (2004) combined a single 50 ks XMM-Newton pointing with an ultra deep radio survey, finding an identification rate of $\sim 33\%$.

In previous papers (El Boucheffry 2009; El Boucheffry 2008; El Boucheffry & Cress 2007), a detailed study on the optical/infrared identifications of FIRST radio sources in Boötes field of the NDWFS survey was performed. A total of 688/900 FIRST radio sources have been identified in one or more bands (*B_w*, *R*, *I*, *K*) in Boötes field. This field covers a large area of about 9.3 square degrees and has been surveyed almost across the full electromagnetic spectrum: in UV (GALEX), optical (NDWFS), infrared (FLAMEX; Elston et al. 2006), radio (VLA/FIRST; Becker, White, & Helfand 1995 and WSRT; de Vries et al. 2002), and X-ray (Murray et al. 2005; Kenter et al. 2005). The X-ray properties of FIRST radio sources have been studied in a few papers. For example, Brinkmann et al. (2000) compiled a large sample of X-ray selected AGN from the ROSAT All Sky Survey (Voges et al. 1999) and cross correlate this sample with the FIRST radio survey, finding a relatively tight linear correlation between the logarithmic of radio luminosity and the X-ray luminosity in the soft X-ray 0.5-2 keV band. At bright flux limits, $f_X(2 - 10 \text{ keV}) = 10^{-13} \text{ erg s}^{-1} \text{ cm}^{-2}$, Akiyama et al. (2000) cross correlated the ASCA Large Sky Survey (LSS) with the FIRST catalogue, finding an identification rate of a $\sim 35\%$ and a fraction of radio loud hard X-ray selected sources of approximately 10%. At faint X-ray flux $f_X(0.5 - 2) \text{ keV} = 1.5 \times 10^{-16} \text{ erg s}^{-1} \text{ cm}^{-2}$, four radio sources from FIRST survey have been identified as a radio counterparts to four X-ray sources in the Large Area Lyman Alpha survey (LALA) Boötes field (wang et al. 2004). Sanchez-Sutil et al. (2006) cross correlated the FIRST radio sources with an ULX (Ultra Luminous X-ray) catalogue, and they found 70 positional coincidence and the majority of them are associated with the galaxy nucleus. The aim of this paper is to shed light on the nature and the environment of the faint radio population (at mJy level) detected in the FIRST radio survey, to characterise their X-ray counterparts and to distinguish between different groups of AGNs. Here,

I combine data from the FIRST radio survey with a new, medium depth (5 ks/pointing) Wide field X-ray survey (known as the Chandra XBoötes) of the Boötes field of the NDWFS survey. The X-ray data reach a limiting flux of $4 \times 10^{-15} \text{ erg s}^{-1} \text{ cm}^{-2}$ in the soft band and $8 \times 10^{-15} \text{ erg s}^{-1} \text{ cm}^{-2}$ in the full band. Compared to the previous studies this data set, the FIRST/XBoötes, has the advantage of deep wide area optical/infrared observations, radio and intermediate in depth X-ray observations.

The paper is organised as follows: section 2 presents a summary on the radio, X-ray and optical data. The matching procedure is described in section 3. Optical morphology and optical magnitude of the radio-X-ray matches are investigated in section 4 and 5 respectively. Section 6 presents the optical classification of the radio-X-ray matches, photometric redshift and also investigates the *K* - *z* diagram. Section 7 investigates the radio-X-ray luminosities. Section 8 presents the X-ray-to-optical flux ratio and Extremely red objects. Section 9 is devoted to the optical and X-ray properties of the radio-X-ray matches. Section 10 presents the final data table, and conclusions are summarised in section 11. Throughout this paper it is assumed that $\Omega_M = 0.3$, $\Omega_\Lambda = 0.7$ and $H_0 = 70 \text{ km s}^{-1} \text{ Mpc}^{-1}$.

2 THE SAMPLE DATA

2.1 The FIRST catalogue

The radio data are from the 2002 version of the FIRST Very Large Array catalogue¹ (Faint Images of the Radio Sky at Twenty-Centimetres; Becker, White, & Helfand 1995), and it is derived from 1993 through 2002 observations. The FIRST radio survey has been carried out in recent years with the VLA in its B-configuration to produce a map of 20 cm (1.4 GHz) sky with a beam size of 5.4 arcsec and an rms sensitivity of about 0.15 mJy/beam. The 2002 version of the catalogue covers a total of about 9033 square degrees of the sky (8422 square degrees in the north Galactic cap and 611 square degrees in the south Galactic cap); and contains 811,117 sources from the north and south Galactic caps. The accuracy of the radio position depends on the brightness and size of the source and the noise in the map. Point sources at the detection limit of the catalogue have positions accurate to better than 1 arcsec at 90% confidence; 2 mJy point sources typically have positions good to 0.5 arcsec. The radio surface density is $\sim 90 \text{ deg}^{-2}$; and about 900 sources fall within the NDWFS Boötes field.

The FIRST survey provides high spatial resolution (5 arcsec beam). As a result, many large radio sources are resolved out and split into multiple components. In order to identify groups of sources that are likely to be sub-components of a single source, an algorithm similar to that used by Magliocchetti et al. (1998) is adopted for identifying genuine double radio sources in the FIRST survey. All doubles with $\theta \leq 10 \sqrt{F_{\text{tot}}}$ are considered as a single object, where θ is their separation in arcsec and F_{tot} is their summed flux density in mJy. The technique is based on the $\theta \propto S$ relation found by Oort (1987). Among the 900 FIRST radio sources that cover the NDWFS survey (Boötes field, 145 (16%) are double, 30 (3%) have three components, 6 (0.6%) sources have four components and 8 (0.8%) sources have more than five components.

¹ The FIRST catalogue is available online at <http://sundog.stsci.edu>

2.2 The XBoötes catalogue

The X-ray data (Murray et al. 2005; Kenter et al. 2005) used in this paper are from the Chandra XBoötes surveys. The XBoötes catalogue contains ~ 3213 X-ray point sources and is publicly available through the NOAO Deep Wide Field Survey (NDWFS) homepage². The Chandra XBoötes survey imaged a large and contiguous area of 9.3 square degrees of the Boötes field of the NDWFS survey, and is centred on RA (J2000) $\sim 14^h 32^m$ and Dec (J2000) $\sim 34^\circ 06'$. The field was observed by the advanced CCD Imaging Spectrometer (AGIS-I) on the Chandra X-ray Observatory, and the data have arcsecond resolution and broad energy response up to 10 keV. The X-ray data was taken in 126 separate pointings, each observed for 5 ks. The X-ray data are filtered in the three energy bands: 0.5 – 7 keV, 0.5 – 2 keV, 2 – 7 keV with a limiting flux of $\sim 8 \times 10^{-15}$ erg s^{-1} cm^{-2} in the full band (0.2 – 7 keV) and of $\sim 4 \times 10^{-15}$ erg s^{-1} cm^{-2} in the soft band (0.5 – 2 keV).

2.3 The NDWFS survey (Boötes field)

The NOAO Deep Wide Field Survey (NDWFS) is a deep multi-band imaging (*B_w*, *R*, *I*, *J*, *H*, *K*) designed to study the formation and evolution of large scale structures (Jannuzi et al. 1999; Brown et al. 2003). This survey consists of two fields³; the first one is located in Boötes field centred on approximately $\alpha = 14^h 30^m 05.7120^s$, $\delta = +34^\circ 16' 47.496''$, covering a 3 by 3 square degrees region, and the latter one is located in a 2.3 by 4 square degrees region in Cetus field. The survey catalogue has been split by declination range into four strips ($32^\circ \leq \delta < 33^\circ$, $33^\circ \leq \delta < 34^\circ$, $34^\circ \leq \delta < 35^\circ$, $35^\circ \leq \delta < 36^\circ$); each strip observed in four bands (*B_w*, *R*, *I*, *K*). The magnitude limits are: *B_w* ~ 25.5 mag, *R* ~ 25.8 mag, *I* ~ 25.5 mag and *K* ~ 19.4 mag.

3 CROSS IDENTIFICATION METHOD

When searching for optical/infrared or X-ray counterparts of radio sources (or vice versa), one must decide on the matching criteria to be adopted. A compromise is required in order to maximise both the completeness (i.e. all potential radio sources are included) and the reliability (i.e. all included identifications are genuine) of the data base. The best way to ensure completeness and reliability is to determine a maximum position offset which includes all possible identifications and to have some realistic estimate of the uncertainties in both the radio and X-ray positions. The FIRST radio survey provides a high positional accuracy that is around $\sim 0.5''$. The rms error of the X-ray positions ranges from 0.0'' to 6.1'' depending on the off-axis angle. The mean uncertainty in the X-ray positions is estimated to be $\sim 1.68''$. Combining these in quadrature with the radio astrometry errors defines a circle about the predicted coordinates of the source; with a radius of 1.75'' (1σ), within which the X-ray counterpart of the radio source is expected to be found.

I first cross correlated both FIRST catalogue and XBoötes based on simple positional coincidence, and then took all the pairs whose radio and X-ray positions differed by less than 20''. The cumulative distribution of the separations in angular distances between the X-ray and radio positions is shown in Figure 1. The upper curve shows the distribution offset for all matches between radio and X-ray positions. The lower curve shows the differential distribution which

would be expected if all identifications were chance coincidence. To estimate the false match rate, all radio sources were shifted by 3', and the source matching algorithm was run again. As clearly seen from the plot, the radio-X-ray offset distribution exceed vastly the random distribution at offset $\leq 2''$, meaning that real identifications of FIRST radio sources with X-ray objects dominate at smaller offsets. Based on this Figure, a 2'' cut-off was chosen as a good compromise that radio and X-ray sources can be considered as counterparts, which results in 92 radio-X-ray matches. Furthermore, only one random identification was made at offsets smaller than the chosen matching radius of 2 arcsec, corresponding to 1% of the true matches.

Figure 2 shows the positional offset between the radio and their X-ray counterparts. There are 86/92 (93%) X-ray-radio matches within 1.5'' and only 6 sources lie beyond 1.5''. It is clearly seen from the figure that the sources are not centered on (0,0) and there is a small systematic offset between the radio and X-ray reference frames. The mean offsets are $\langle \Delta Ra \rangle = -0.32''$ and $\langle \Delta Dec \rangle = -0.27''$. I shifted the X-ray reference frame to match up to the radio using the median offset of matched objects and again ran the source matching algorithm. Correcting this small offset made no difference to the total matched sample. Bauer et al. (2002), used a 1'' search radius for the VLA/Chandra cross correlation on the HDF-N; Barger et al. (2007) adopted a 1.5'' search radius as a good compromise for the VLA/HDF-N.

The comparison of the positions of FIRST radio sources with the XBoötes X-ray sources reveals 92 coincidence, corresponding to an identification rate of $\sim 10\%$ (92/900). This clearly shows that there is little overlap between radio and X-ray sources. A higher overlap between radio sources and X-ray sources has been found by Tozzi et al. (2009). In their cross correlation between radio sources and X-ray sources in the E-CDFS area, they found that 40% of the radio sources are associated with X-ray sources. Rovilos et al. (2007) found that the radio detection rates for the E-CDFS and CDFS X-ray sources increases from 9% to 14% in the central region of this field (which has deeper X-ray data), while the X-ray detection rates for radio sources are 21% for the E-CDFS and 33% for the CDFS field. The radio flux density limit in Tozzi et al. (2009) ranges from 42 μ Jy at the field center, to 125 μ Jy near the field edge and in Rovilos et al. (2007) is 60 μ Jy, while the detection threshold in the FIRST survey is 1 mJy. Ciliegi et al. (2003) reported a high fraction of 36% in the HELLAS field. The identification rate measured in Akiyama et al. (2000) is 35% for the FIRST radio sources in the LSS field ($f_X(2.0 - 10\text{keV}) = 1 \times 10^{-13}$ erg s^{-1} cm^{-2}). It is interesting to note that both radio and X-ray detection rates increases with deeper observations. Ciliegi et al. (2003) have shown that the radio-X-ray association is a function of the radio/X-ray limit ratio, f_r/f_X (see their table 2), the deeper radio data compared to the X-ray flux limit, the higher the number of radio-X-ray associations. To summarise, the small fraction of radio detected X-ray sources in comparison to the previous results is due to a mismatch between the flux limit of the VLA FIRST 1.4 GHz (deep radio survey) and that of the Chandra XBoötes survey (shallow X-ray survey).

3.1 Optical counterparts to the radio/X-ray matches

Brand et al. (2006) presented a catalogue of the optical/infrared counterparts to the 3213 X-ray point sources detected in the

² <http://www.noao.edu/noao/noadeep/XBootesPublic/index.html>

³ <http://www.noao.edu/noao/noadeep/>

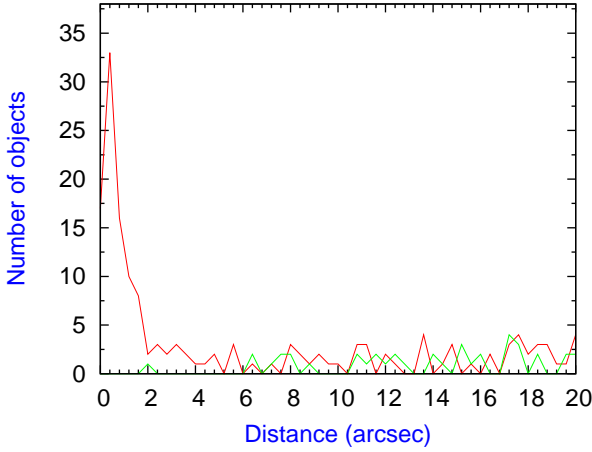


Figure 1. Distribution of angular distances between radio and X-ray positions (top line). The lower plot shows the expectation of chance associations as a function of angular separation. Sources are considered to be associated if the separations are ≤ 2 arcsec.

XBoötes survey⁴. These authors found optical counterparts for 98% of the X-ray sources using a Bayesian identification scheme. For each candidate the full catalogue provides a number of parameters containing information about the X-ray sources and their optical/infrared counterparts. A detailed analysis of the matching criteria and a full description of the catalogue is presented in Brand et al. (2006). The following provides a brief description of the parameters that have been taken into account in this analysis:

- nopt: labels the number of optical sources with $> 1\%$ probability of being the correct optical/infrared counterparts to the X-ray source in the case of multiple matches.
- oprank: labels the optical rank when the X-ray sources are multiply matched. This parameter ranges from 1 (most probable) in running order to the least probable.
- bayprob: gives the Bayesian probability of an optical object being the true counterpart to an X-ray source.
- Class: describes the optical morphology of the optical counterparts to the X-ray sources (1: point-like object; 0: galaxy (extended or resolved)).
- flag: In cases of no optical ID being the most probable identification, the flag parameter takes three values which have been applied manually (Brand et al. 2006):

- flag = -3: no optical ID but source obscured by nearby star / missing data.
- flag = -2: no optical ID, but X-ray position is close to optically bright galaxy (source is either obscured by or associated with the galaxy).
- flag = -1: 'true' no optical ID (optical image is truly blank).

A total of 90/92 of the X-ray counterparts to FIRST radio sources have optical counterparts and the remaining two X-ray sources are associated with a blank field (flag = -1). The majority (75%) of the X-ray candidates are associated with only one optical object (nopt=1). In 22 cases, the X-ray candidates have more than one optical match. Ten X-ray sources have 2 multiple matches,

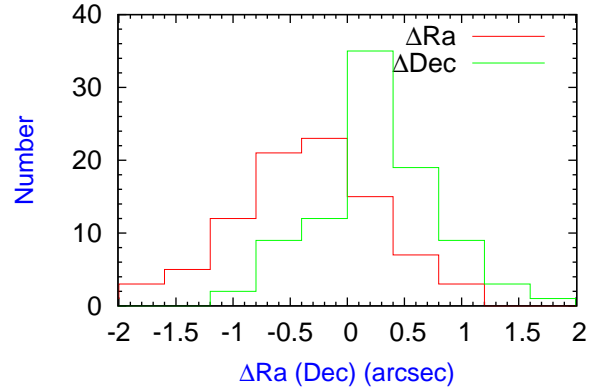
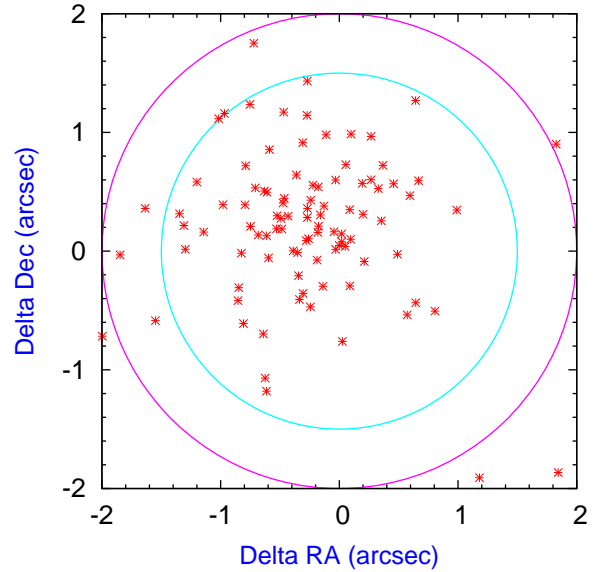


Figure 2. Diagram of the offset in Ra and Dec (arcsec) of the FIRST radio sources and XBoötes sources with a $2''$ and $1.5''$ circles overlaid to show how many of the matches are separated by more than $2''$. Lower panel: offset histograms for ΔRa (solid histogram) and ΔDec (dashed histogram).

three X-ray candidates have three multiple matches, five X-ray sources are associated with 4 optical objects, one source have 5 optical counterparts, two X-ray candidates have 6 counterparts and one have 8 possible matches. In those multiple matches, only sources with oprank = 1 (high probability) have been considered as real matches.

In El Bouchefry (2008), I have presented a cross correlation of FIRST radio sources and the NDWFS survey (Boötes field), using both the likelihood ratio and a simple positional coincidence. The identification procedure yielded 688/900 optical counterparts to FIRST radio sources in either one or more bands (B_w , R , I , K). From these, 79 optical/infrared sources are common between the X-ray detected and radio detected samples. One should note that the Boötes field is split by declination into four strips ($32^\circ < \delta \leq 33^\circ$, $33^\circ < \delta \leq 34^\circ$, $34^\circ < \delta \leq 35^\circ$, $35^\circ < \delta \leq 36^\circ$), each is imaged in four bands (B_w , R , I , K). The Boötes field is partially covered in K band (especially the second strip and there

⁴ The catalogue can be obtained through the NDWFS homepage at <http://www.noao.edu/noao/noaodeep/XBootesPublic>

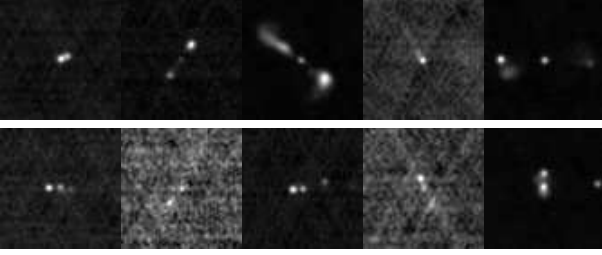


Figure 3. The FIRST radio sources with multiple components identified by the selection algorithm (Magliocchetti et al. 1998). Each FIRST stamp is $2' \times 2'$, normalised to the maximum intensity.

is no K data for the first strip). In El Boucheffry (2008), I cross correlated the FIRST radio sources and the FLAMEX survey (Elston et al. 2006) in order to get infrared data (K and J) for the second strip. FLAMEX survey covers about 4.7 deg^2 of the Boötes field.

Among the 79 radio-X-ray matches, 4 double-radio sources are identified in XBoötes field, four radio sources with three components and one source with four components. But only one component of each group that is identified in the XBoötes field, Figure 3 shows images of the identified double radio sources recognised by the selection algorithm. These images are extracted from the FIRST website⁵.

In summary, the cross correlation of FIRST radio sources and the XBoötes survey yielded a total of 92 radio-X-ray associations. A total number of 79 optical/infrared sources is common to both radio and X-ray samples.

4 STELLARITY

Optical morphologies of these objects provide a further clue as to their nature. Here, I performed a simple morphological analysis of the identifications using the SExtractor stellarity parameter (Bertin & Arnouts 1996); which has values between 0 (galaxies or resolved) and 1 (stars or unresolved). The SExtractor software has difficulty in correctly classifying sources fainter than $R = 23$ in the NDWFS data (Brown et al. 2003; Brand et al. 2006). Typically, all objects brighter than $R \sim 23$ should be classified correctly. Beyond that magnitude the SExtractor cannot give a reliable classification and just assign random values between 0 and 1. Figure 4 illustrates the stellarity parameter against the apparent R -band magnitude for all the X-ray sources identified in Boötes field in the upper panel, and for all radio-X-ray matches in Boötes field in the lower panel. If all sources with stellarity ≥ 0.7 are classified as point-like and all sources with stellarity < 0.7 (extended) as galaxies, there are 33 (42%) optical point-like sources and 46 (58%) galaxies. Taking a crude split between stars and galaxies at stellarity level of 0.9 and 0.1 for stars and galaxies respectively; all sources with stellarity ≥ 0.9 are classified as point-like objects (mostly QSO), sources with stellarity ≤ 0.1 as galaxies and intermediate objects as sources with $0.1 < \text{stellarity} < 0.9$. This criterion yielded 27 (34%) point-like sources, 35 (44%) galaxies and 17 (22%) intermediate sources.

The R band images for all the radio-X-ray matches are shown in Figure 5. These cut-out images have been obtained from

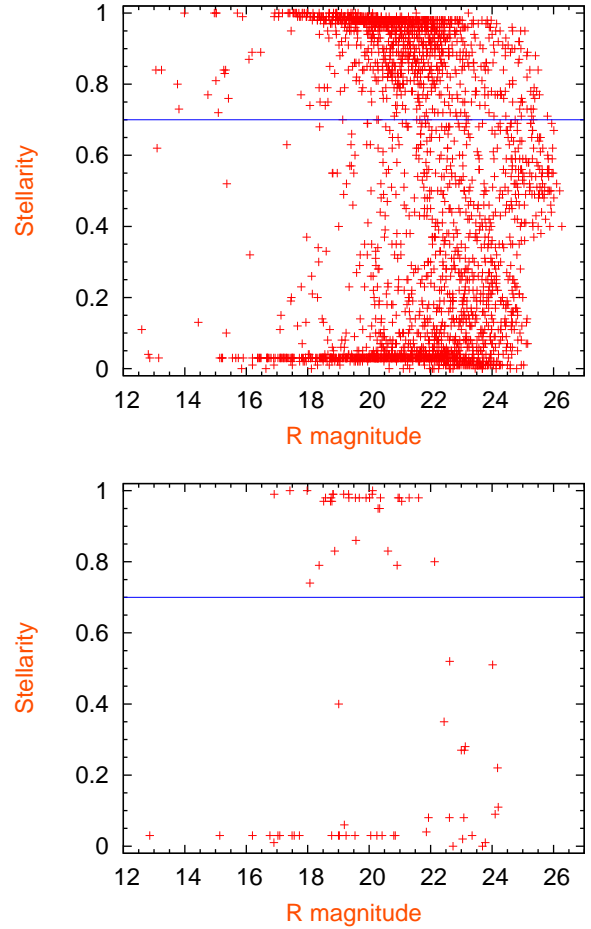


Figure 4. The SExtractor stellarity parameter (Bertin & Arnouts 1996) versus R -band magnitude for the X-ray sources identified in Boötes field is shown in the top panel and for optical counterparts to the radio X-ray matches in the bottom panel. The horizontal line shows the boundary that has been assumed to classify the radio-X-ray matches into point sources (stellarity ≥ 0.7) and extended sources (stellarity < 0.7). Stellarity varies from 0 for a galaxy to 1 for a star.

the NOAO cut-out service: <http://archive.noao.edu/ndwfs/cutout-form.html>. The majority (63/75; 84%) of the radio-X-ray matches have magnitudes brighter than $R = 23$ from which 57% (36/63) have magnitudes brighter than $R = 20$ mag. These sources appear to be mainly elliptical, and some lenticulars are also seen. A number of these sources also appear to be either interacting or merging galaxies. At fainter magnitudes, the sources tend to have low stellarity (see Figure 4), so they are likely QSOs or compact galaxies.

5 OPTICAL MAGNITUDE DISTRIBUTIONS

In the absence of spectroscopic data, the magnitude and colour distributions of the optical counterparts can be used to derive some information on the nature of the faint radio population. In Figure 6, the optical magnitude distributions in R band of the optical counterparts to the radio-X-ray matches are plotted. The histograms shown are (from top to bottom) distributions for: 1) all X-ray sources optically identified in the Boötes field, 2) all X-ray sources identified in four bands (B_w , R , I , K) in the Boötes field, 3) all FIRST radio sources identified in the Boötes field, and 4) all the optical counter-

⁵ <http://third.ucllnl.org/cgi-bin/firstcutout>

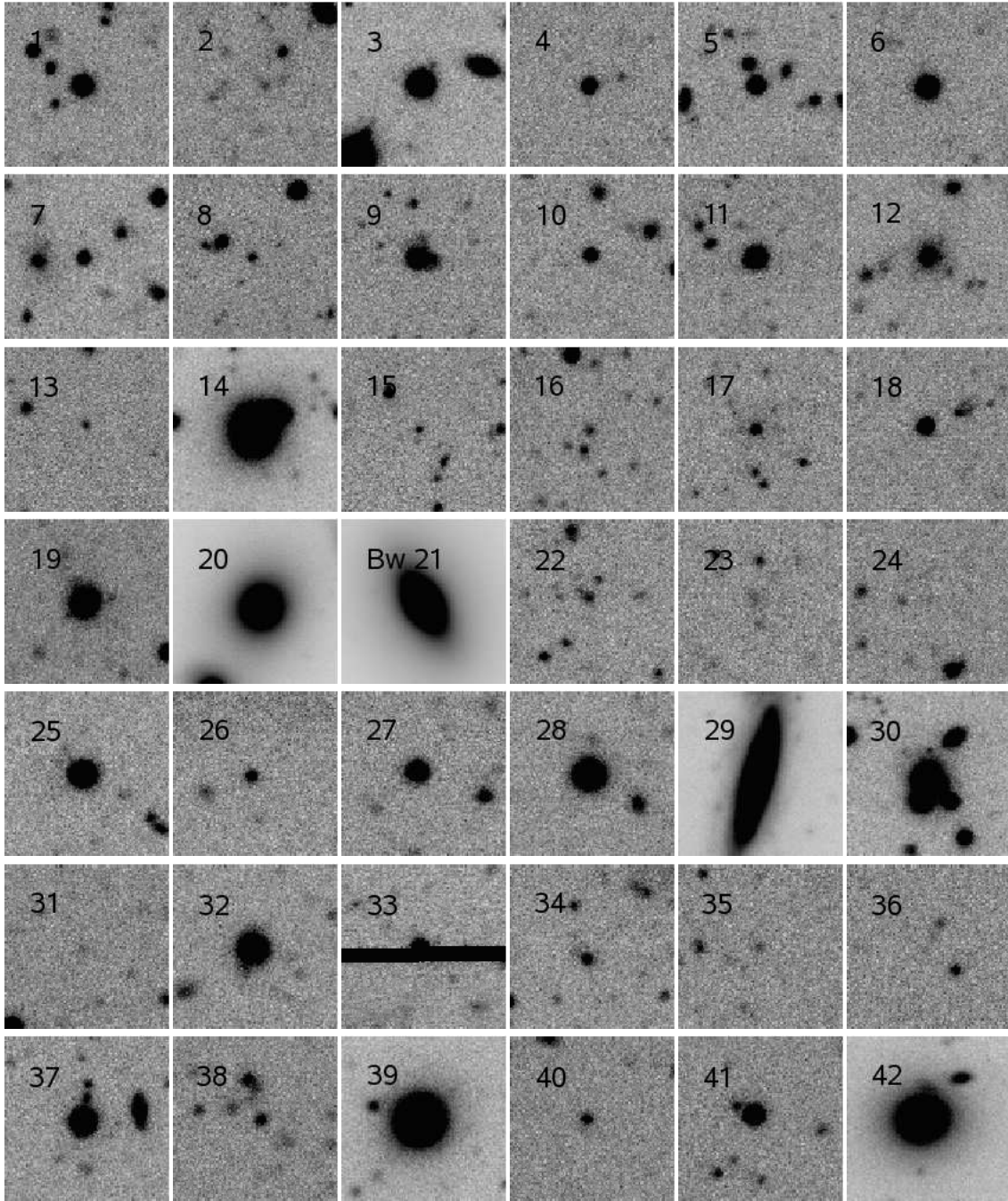


Figure 5. The R band images ($2' \times 2'$) of all the 79 radio-X-ray matches in the 9.3 deg^2 Boötes field. All the images are centred on the FIRST radio sources. The FIRST radio sources reference number (shown in column 1 of Tables 1 and 2) is at the top left of each image. These cut-out images have been obtained from the NOAO cut-out service: <http://archive.noao.edu/ndwfs/cutout-form.html>.

parts to the radio-X-ray matches. The magnitude distribution of all X-ray sources identified in Boötes field has two apparently weak peaks with a small tail at brighter magnitudes and few counterparts at fainter magnitudes. The radio sample has significantly flatter distributions compared to the global optical catalogue (orange histogram) and to the X-ray sources identified in four bands (green histogram), and falls off at $R \sim 24$. The mean magnitude of the optically extended radio-X-ray matches is $R = 20.68$ with a median of 19.91. For radio-X-ray matches that are associated with point-like objects the mean magnitude is $R = 19.62$ and the median is 18.58.

The mean magnitude for all radio-X-ray matches is $R = 20.16$ and the median is $R = 22.13$.

6 PHOTOMETRIC REDSHIFTS

6.1 Optical classification

Optical spectroscopic information is available for 22 out of 79 sources (28%). The spectroscopic data have been obtained from

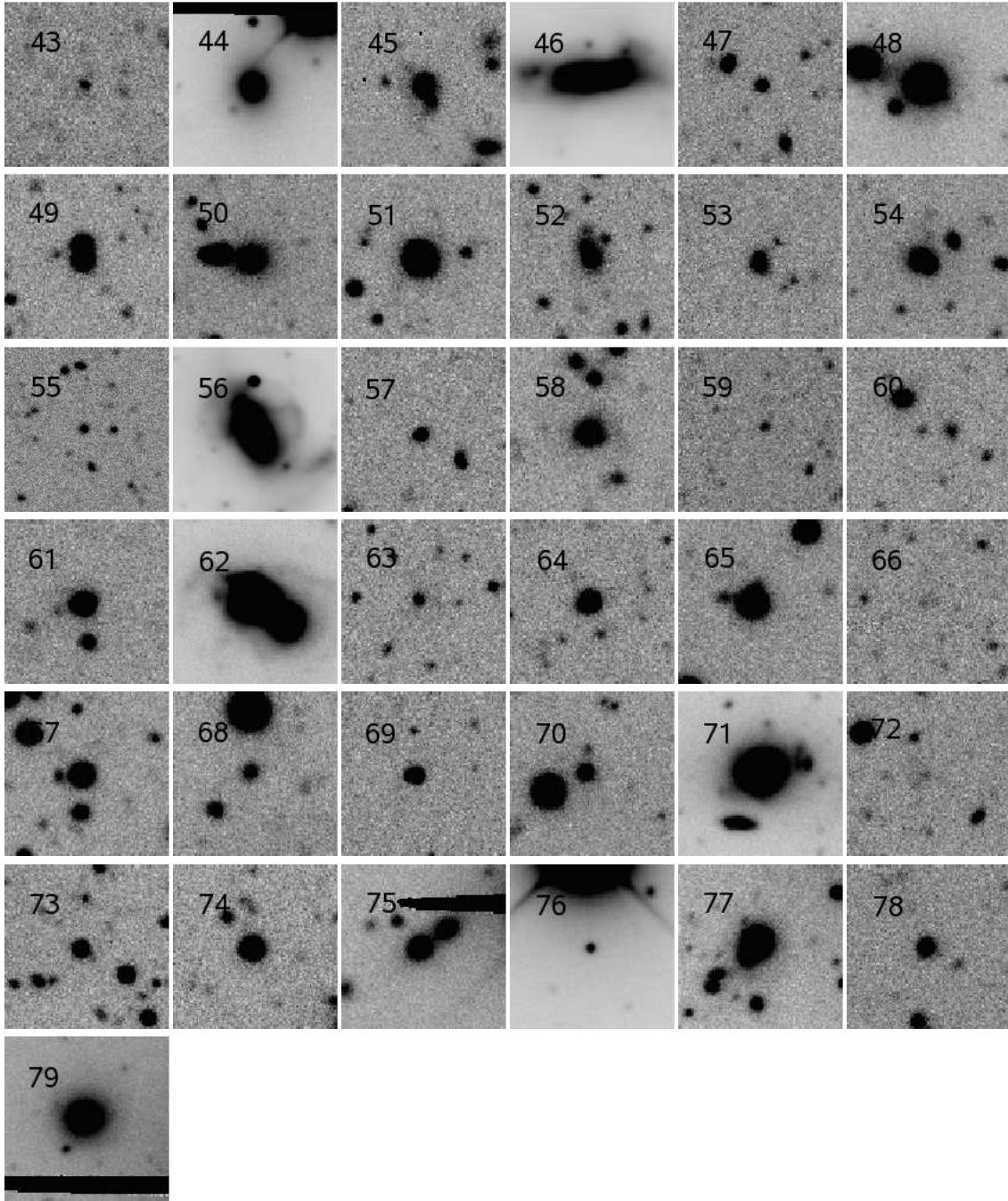


Figure 5 – continued

the SDSS (Sloan Digital Sky Survey). The spectroscopically identified sample comprises 14 point-like objects (13 sources show broad emission lines and one source shows a featureless spectrum) and 8 resolved radio galaxies (with emission/absorption lines). Extragalactic radio sources are known to be a mixture of two main populations: AGN and star-forming galaxies. The AGN class can be divided into two sub-classes: QSOs (often unresolved in the optical image) and objects where the AGN does not dominate the entire SED (Spectral Energy Distribution), such as type 2 QSOs, low luminosity AGN (seiyfert and LINER) and absorption line AGN. A total number of 13 point-like objects are spectroscopically classified as QSOs by the SDSS and the point-like source

which shows a featureless optical spectrum could be classified as a BL Lac object. The presence of broad emission lines (width larger than 2000 km/s) like Mg_{II} , C_{III} and at large redshifts C_{IV} and $Ly\alpha$ classifies the source as a broad line AGN (BLAGN), type -1 AGN or QSO according to the simple unification model by Antonucci (1993). To classify emission line galaxies as star-forming or AGN, I used the line flux ratio diagram of $[O_{III}]/H\beta$ versus $[N_{II}]/H\alpha$ (BPT diagram, Baldwin et al. 1981). I used an empirical criterion to segregate AGN host galaxies from star-forming galaxies: $[O_{III}]/H\beta = 0.61/([N_{II}]/H\alpha - 0.05) + 1.3$ given by Kauffmann et al. (2003). With these diagnostics, the AGN population still remained mixed. To distinguish seiyferts from LIN-

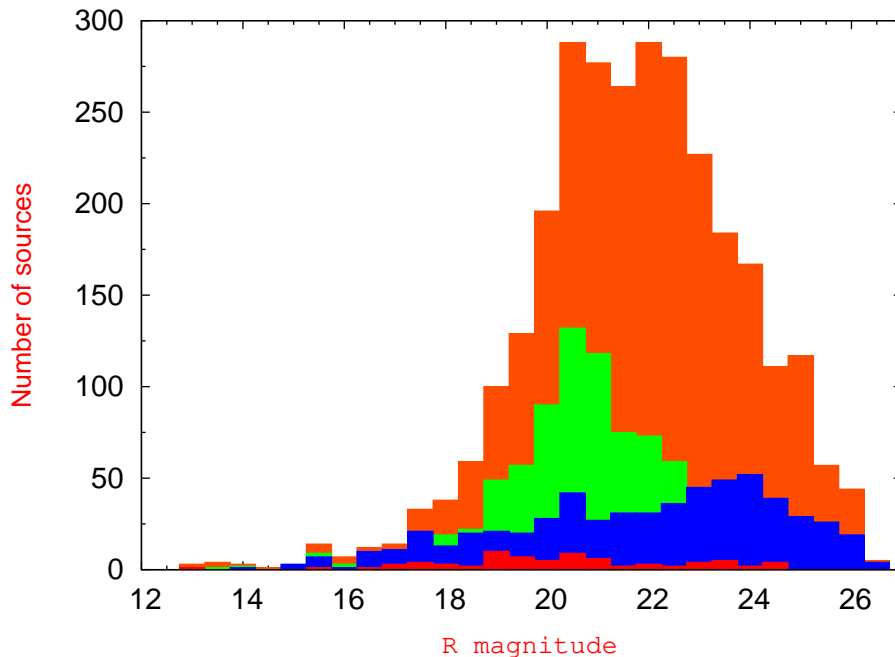


Figure 6. The optical magnitude distributions in R band for (from top to bottom): all the X-ray sources identified in Boötes field, all X-ray sources identified in four bands (Bw , R , I , K) in Boötes field, all FIRST radio sources identified in Boötes field and all the common optical counterparts to the radio-X-ray matches.

ERS I used an empirical relation given by Kewley et al. (2006): $[\text{O}_{\text{III}}]/\text{H}\beta = 1.18 [\text{O}_{\text{I}}]/\text{H}\alpha + 1.3$. Based on the 2 independent classification of galaxies, 3 emission lines galaxies were classified as star-forming galaxies (sources # 42, #46, #71) and four were classified as LINERS (sources #29, #39, #56, #62).

In Summary, among the spectroscopically classified sources I find: 13 BLAGNs (59% of the sample with spectroscopic redshift), one BL Lac object (source #11), 3 (14%) star-forming galaxies and four (18%) LINERS galaxies. The optical spectra of these sources are shown in Figure 19 with spectroscopic redshift, type and source number printed on each figure. One also notes the fair agreement (98%) between the SDSS classification and the SExtractor stellarity parameter (provided by the NDWFS catalogue) used so far to classify the radio-X-ray matches into point-like objects and extended objects. For the remaining sources (55) without spectroscopic information I turn to photometric redshift techniques to estimate redshifts for these.

6.2 Photometric redshift technique

Photometric redshift techniques have been applied by many authors to obtain photometric redshift for X-ray sources identified in optical/radio surveys (Barger et al. 2001, 2002; Gandhi et al. 2004; Georgakakis, et al. 2004; Mobasher et al. 2004; Zheng et al. 2004). X-ray sources may have complex spectral energy distributions that arise from both the host galaxy and the AGN. Consequently estimating photometric redshifts for X-ray sources using templates for normal galaxies may be problematic. However, with the aim of studying the X-ray spatial correlation function in the NDWFS survey (Boötes field), and in the absence of spectroscopic redshifts, Gonzalez & Maccarone (2002) have studied the effectiveness of photometric redshifts based on galaxy spectral template fitting for 65 X-ray luminous objects detected by Chandra in the Caltech Faint Galaxy redshift survey (CFGRs). The authors used the two publicly

available codes, *Hyperz*⁶ (Bolzonella, Miralles & Pello 2000) and BPZ (Bayesian photometric redshift, Benitez 2000). Gonzalez & Maccarone (2002) have shown that the two codes produce similar results when compared to spectroscopic data, and confirm that photometric redshifts based on template fitting for X-ray sources are quite robust for 90% of sources that have optical counterparts brighter than $R \sim 24.5$ (see also Barger et al. 2002; Gandhi et al. 2004; Zheng et al. 2004). They have shown that photometric redshift estimates agree well with spectroscopic measurements for objects in which galactic light dominates the optical flux. Using multi-wavelength photometric data from the Great Observatories Origins Deep Survey, Mobasher et al. (2004) also attempted to estimate photometric redshifts for a sample of 434 galaxies with spectroscopic redshifts in the Chandra Deep Field-South with magnitudes in the range $18 < R_{AB} < 25.5$. The authors have applied a Bayesian method to two subsamples of galaxies: Extremely Red Objects (EROs) and AGNs. Mobasher et al. (2004) found good agreement between photometric redshifts based on template fitting and more accurate results for EROs when compared to the sample as a whole ($\sigma = 0.051$), while the results tended to be less accurate for X-ray sources (AGNs) ($\sigma = 0.104$), but still acceptable for further studies.

In this paper, I used the publicly available code *Hyperz* to obtain photometric redshifts for the radio-X-ray matches. The code is based on fitting template spectral energy distributions (SEDs) to broad band photometry fluxes in as many filters as possible. I used Gissel 98 galaxy templates which are the 1998 update of the spectral synthesis models described by Bruzual & Charlot (1993), with different star formation histories and spanning a wide range of ages from 1 Gyr to 30 Gyrs. All the models include solar metallicity and Miller (1979) initial mass function. The *Hyperz* code also includes Lyman forest absorption according to the model of Madau (1995).

⁶ The code is publicly available at: <http://webast.ast.obs-mip.fr/hyperz/>

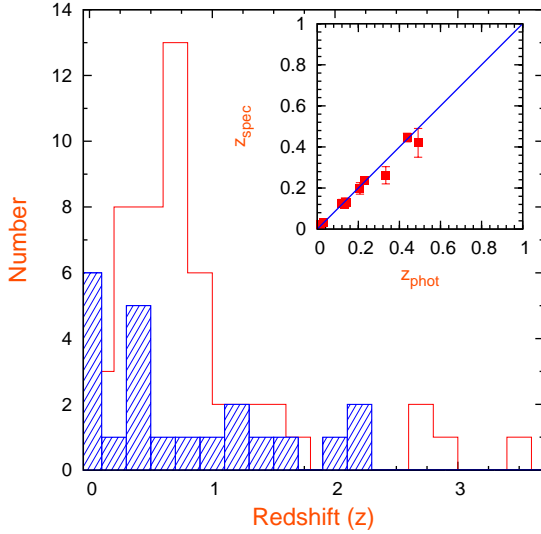


Figure 7. Photometric redshift distribution for the common optical counterparts to the radio-X-ray matches (open histogram) and spectroscopic redshift distribution for 22 radio-X-ray matches (hatched regions). The inset shows the z_{phot} vs. z_{spec} . The solid line is the one-to-one relation.

Four quasars templates compiled from Le PHARE software⁷ (Cristiani & Vio 1990; Cristiani et al. 2004) were included as well. For each identified radio-X-ray source *Hyperz* provides a possible z_{phot} (and corresponding reduced χ^2 probability) for each set of templates. The “best” highest probability ($\chi^2 \leq 2.7$, 90% confidence limit) was selected as the correct one, together with the corresponding spectral type.

Four filters (B_w , R , I , K) have been used to obtain photometric redshifts for 79 radio-X-ray matches. The majority of the radio-X-ray matches (63%) were detected in four bands. As mentioned previously, no infrared data were available for the first strip ($32^\circ \leq \delta < 33^\circ$), 8 radio-X-ray sources were identified in this strip. In this case, spectroscopic redshift was available for four radio-X-ray matches, and for the remaining four sources, photometric redshift was estimated based on three filters (B_w , R and I). In 23 cases, it was not possible to assign an accurate photometric redshift ($\chi^2 > 2.7$, 90% confidence limit), but 12/23 of these sources have spectroscopic redshifts (The majority of these sources were detected either in three bands or two bands). Figure 7 displays the photometric redshift distribution derived for the radio-X-ray matches. The hatched histogram shows the spectroscopic redshift distribution for 22 radio-X-ray matches and the open histogram displays the best estimate of photometric redshifts ($\chi^2 < 2.7$, 90% confidence limit) as derived from *Hyperz*. The inset shows the photometric redshift vs spectroscopic redshift for sources with secure redshift (i.e. $\chi^2 < 2.7$). About 72% of the sources are estimated to be at $z \leq 1$ with a small tail extending up to $z \sim 4$, and the mean photometric/spectroscopic redshift is $z \sim 0.85$. Only a small fraction (22/79) of the optical counterparts to the radio-X-ray matches have a spectroscopically measured redshift. Comparing the z_{phot} with z_{spec} , the accuracy of the photometric redshift technique applied so far is estimated to be $\Delta z / (1 + z_{\text{spec}}) \approx 0.017$.

⁷ http://www.lam.oamp.fr/arnouts/LE_PHARE.html

6.3 The $K - z$ diagram

It is believed that powerful radio galaxies and quasars are associated with the most massive galaxies at a wide range of redshifts. A number of studies of these objects have shown that the near infrared K band magnitudes follow a tight correlation with redshifts (e.g. Willott et al. 2003; Jarvis et al. 2001). Studies of fainter radio sources at mJy level also have shown a remarkably tight correlation between the K magnitude and redshift (e.g. Brookes et al. 2006; El Boucheffry & Cress 2007). This diagram has been widely used to study evolution of galaxies at high redshifts and is known to be an excellent tool to measure stellar masses of galaxies up to high redshifts. The K magnitude versus redshift of the optical counterparts to the radio-X-ray matches is shown in Figure 8; point-like objects (QSO, stellarity ≥ 0.7) are represented by empty circles, small filled circles stand for resolved objects (galaxies; stellarity < 0.7). Large blue circles denote spectroscopically identified sources, and large yellow circles stand for sources with $R - K > 5$. The blue curve shows the best fit to the $K - z$ relation for the radio-X-ray matches (only extended objects were considered in this fit):

$$K = 17.52 + 4.32 \log_{10} z, \quad (1)$$

and the green line illustrates the second order polynomial best fit of Willott et al. (2003): $K = 17.37 + 4.53 \log_{10} z - 0.31(\log_{10} z)^2$. The three upper lines show the passive stellar evolutionary tracks of an $L_*(K)$ galaxy (where $L_*(K)$ is the K band L_*) for an instantaneous starburst at $z = 5$ and $z = 10$ as well as a no-evolution curve, as derived by Jarvis et al. (2001). The majority of the sources lie brighter than L_* . But it is important to note that the K band catalogue is not as deep compared to the study of Willott et al. (2003). Willott et al. (2003) obtained complete K -band data of the complete radio samples. Here there are 28 sources that are not identified in the K band, thus with a sample biased such as this the sources will all tend to be at the bright end of the magnitude range and this could be misleading. However, it is encouraging that the K -band magnitudes with the photometric redshifts agree with the Willott et al. (2003) relation.

7 X-RAY AND RADIO LUMINOSITIES

In the following subsection, the photometric redshift estimates have been used to calculate the X-ray and radio luminosities. The spectroscopic redshift measurements have also been used whenever available.

7.1 X-ray luminosity

Figure 9 displays the X-ray (0.5 – 7) keV luminosity (upper panel) as a function of redshift. The curve represents the detection limit. The rest-frame X-ray luminosity was calculated from:

$$L_X = 4 \pi d_L^2 f_X (1 + z)^{-2+\Gamma} \text{ erg s}^{-1}, \quad (2)$$

where d_L is the luminosity distance (in cm), f_X is the observed full X-ray flux (in $\text{erg s}^{-1} \text{cm}^{-2}$). Γ is the photon index assumed to be $\Gamma = 1.8$ for all sources. Barger et al. (2002), have shown that the use of individual indices result in only small differences in the rest-frame luminosities (see also Barger et al. 2007).

In order to classify the X-ray counterparts to FIRST radio sources, I used the same procedure adopted by Szokoly et al. (2004). Following Szokoly et al. (2004) the X-ray sources can be classified based only on their observed X-ray L_X properties and the hardness ratio, $\text{HR} = h - s / h + s$, where h is the number of counts

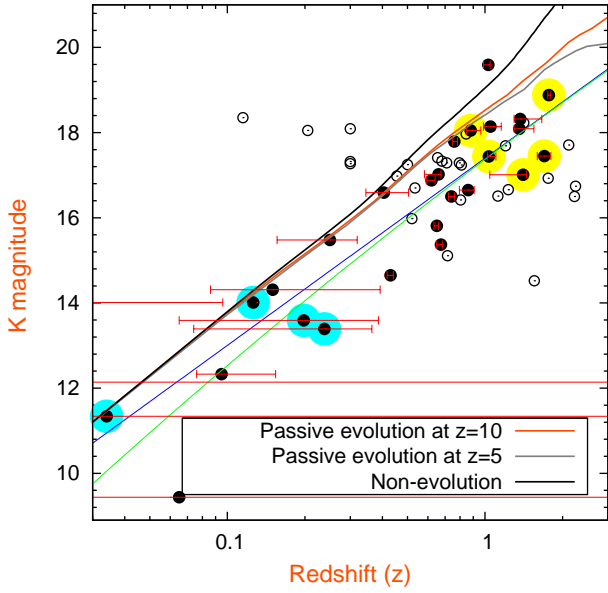


Figure 8. The K magnitude versus redshift z for all the radio-X-ray matches. Point-like objects (QSO, stellarity ≥ 0.7) are represented by empty circles, small filled circles stand for resolved objects (galaxies; stellarity < 0.7). Large blue circles denote spectroscopically identified sources, and large yellow circles stand for sources with $R - K > 5$. The green line shows the best fit to $K - z$ relation of Willott et al. (2003) and the blue line shows the best fit $K - z$ relation for only AGNs with $\log f_X/f_{opt} > 1$ for this study (point sources are not included in this fit). The three upper lines show the passive stellar evolutionary tracks of an $L_*(K)$ galaxy (where $L_*(K)$ is the K band L_*) for an instantaneous starburst at $z = 5$ and $z = 10$ as well as a no-evolution curve, as derived by Jarvis et al. (2001).

detected in the 2 – 7 keV band and s is the number of counts detected in the 0.5 – 2 keV band. The X-ray luminosity L_X is derived from the 0.5 – 7 keV fluxes and spectroscopic/photometric redshifts. The criteria adopted by Szokoly et al. (2004) are as follows:

- (i) Galaxy: $L_X \leq 10^{42}$ erg. s $^{-1}$ with hardness ratio $HR < -0.2$.
- (ii) AGN-2: $10^{41} \leq L_X < 10^{44}$ erg. s $^{-1}$ and the hardness ratio $HR > -0.2$.
- (iii) AGN-1: $10^{42} \leq L_X < 10^{44}$ erg. s $^{-1}$ and the hardness ratio $HR \leq -0.2$.
- (iv) QSO-2: $L_X > 10^{44}$ erg. s $^{-1}$ with hardness ratio $HR > -0.2$.
- (v) QSO-1: $L_X > 10^{44}$ erg. s $^{-1}$ with hardness ratio $HR < -0.2$.

The classification criteria yielded 37 radio-X-ray matches classified as AGN-1, 19 classified as AGN-2. Normal galaxies represent a small fraction of 9 sources while 12 sources were classified as QSO-1 and 10 sources of these were spectroscopically classified as QSOs and some of these sources were also identified in the ROSAT. The QSO-2 type constitutes the smallest fraction: two candidates were classified as QSO-2 sources. Only a few sources considered as the prototype of type 2 quasars have been detected for example in Norman et al. (2002) and Stern et al. (2002b), but many more have been discovered recently (e.g. Fiore et al. 2008).

As discussed previously, different types of X-ray sources are separated in the plot of X-ray hardness ratio versus X-ray luminosity. This trend is shown in Figure 10, where the hardness ratio as a function of the soft X-ray luminosity is illustrated in the top panel and as a function of the hard X-ray luminosity in the lower panel.

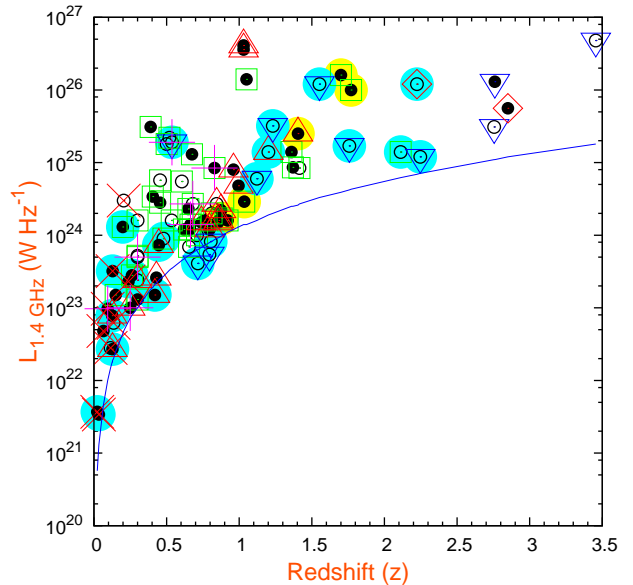
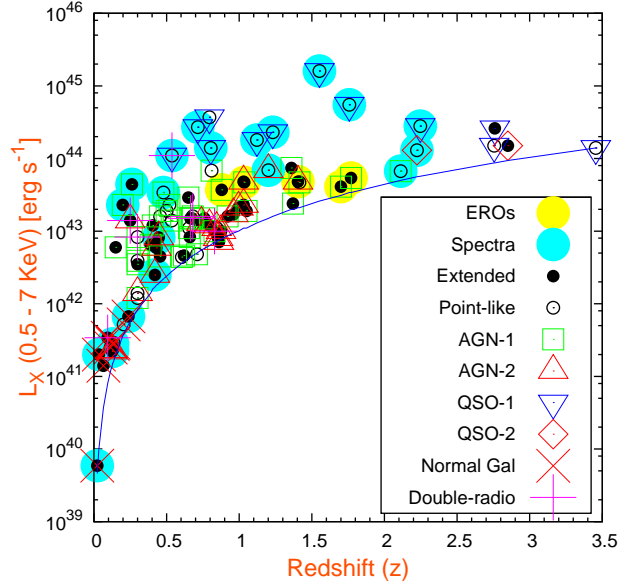


Figure 9. Full (0.5 – 7) keV X-ray luminosity versus redshift for the radio-X-ray matches is shown in the top panel. Solid line represents the faintest limiting X-ray luminosity for a source with a full flux of $\sim 8 \times 10^{-15}$ erg s $^{-1}$ cm $^{-2}$ as a function of redshift. The lower panel shows the radio luminosity as a function of redshift for all the radio-X-ray matches and the solid line corresponds to the radio flux limit of 1 mJy. Sources with spectroscopic redshift are shown with large filled circles (Cyan colour).

7.2 Radio luminosity

The rest-frame radio luminosity density was calculated from the following equation:

$$L_{1.4\text{GHz}} = 4\pi d_L^2 S_{1.4\text{GHz}} (1+z)^{-1+\alpha} 10^{-33} \text{ W Hz}^{-1}, \quad (3)$$

where d_L is the luminosity distance (in cm), $S_{1.4}$ is the 1.4 GHz flux density (in mJy), and α is the radio spectral index ($f_\nu \propto \nu^{-\alpha}$), which is taken to be 0.8. Figure 9 (bottom panel) shows the 1.4 GHz luminosity as a function of redshift for all the radio-X-ray matches. Here the curve represents the detection limits. Many of the objects

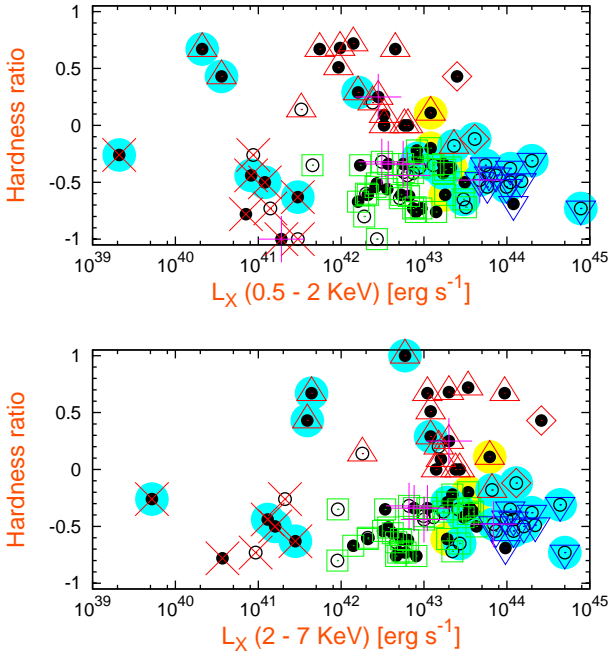


Figure 10. The hardness ratio as a function of the soft X-ray luminosity (top panel) and the hard X-ray luminosity (bottom panel) for the radio-X-ray matches. Same symbols as for the radio-X-ray matches in Fig 9.

are close to the lower radio flux limit and also many of the AGN-1 cluster around a redshift of $z \sim 0.7$.

7.3 X-ray-radio correlation?

At the sub-mJ and μ Jy levels, radio emission is known to be a highly accurate indicator of star formation rate (see the review by Condon 1992) because of the extremely tight FIR-radio correlation, which deviates by less than a factor of two over five orders of magnitude. A number of studies have investigated the radio-derived SFRs and found them to be in good agreement with the FIR derived values (e.g. Condon, Anderson & Helou 1991; Haarsma et al. 2000; Hopkins et al. 2001; Bell 2003). The disadvantage of this method is that it is hard to account for the contamination of the radio flux by AGNs. Moreover, star-forming and spiral galaxies are also found to be powerful X-ray emitters with luminosities that sometimes exceed $\approx 10^{42}$ erg s $^{-1}$ (e.g. NGC 3265; Moran et al. 1999). This is believed to be due to a number of high mass X-ray binaries, young supernovae remnants and hot gas plasma associated with star forming regions (see the review by Fabbiano 1989). With the latest generation of X-ray satellites such as Chandra and XMM, it is now possible to study the X-ray-SFR correlation (Bauer et al. 2002; Franceschini et al. 2003; Grimm, Gilfanov & Sunyaev 2003; Ranalli, Comastri & Setti 2003). Early results show good agreement with FIR and radio estimates of the SFR.

Correlations between X-ray and radio luminosities for radio-quiet AGN have been determined by Brinkmann et al. (2000). These authors have cross correlated the FIRST radio survey ($S_{1.4\text{GHz}} > 1\text{mJy}$) and the ROSAT ($f_X > 10^{-13}$ erg m $^{-2}$ s $^{-1}$) and shown that the X-ray and radio luminosities for radio quiet AGN follow a relatively tight linear correlation in the form:

$$\log(L_X) = (-4.57 \pm 2.55) + (1.012 \pm 0.083) \log(L_{1.4\text{GHz}}) \quad (4)$$

Simpson et al. (2006) have converted the previous correlations (found for X-ray-radio AGN) to relationships between fluxes in the form of :

$$S_{0.5-2\text{keV}} (\text{W m}^{-2}) = 10^{-15.5} S_{1.4\text{GHz}} (\text{mJy}) \quad (5)$$

$$S_{2-10\text{keV}} (\text{W m}^{-2}) = 10^{-15.3} S_{1.4\text{GHz}} (\text{mJy}), \quad (6)$$

and also converted correlations found for X-ray radio star-forming galaxies into relations between fluxes:

$$S_{0.5-2\text{keV}} (\text{W m}^{-2}) = 10^{-18} S_{1.4\text{GHz}} (\text{mJy}) \quad (7)$$

$$S_{2-10\text{keV}} (\text{W m}^{-2}) = 10^{-18} S_{1.4\text{GHz}} (\text{mJy}), \quad (8)$$

and used these relations in their plot of X-ray flux versus radio flux density in order to determine the nature of their radio-X-ray matches, depending on which of the two correlations they are closer to (radio quiet AGNs or starburst galaxies). The authors suggest that 20% or more of the radio sources in the sample with $100 \mu\text{Jy} < S < 300 \mu\text{Jy}$ are radio quiet AGNs. They also claim that the radio-X-ray correlation found for radio quiet AGN might be biased to unusually high X-ray-luminous sources because it is derived from cross correlation of a deep radio catalogue (FIRST) and a shallower X-ray survey (ROSAT).

The top panel in Figure 11 presents the distribution of the full X-ray flux against radio flux density. It is immediately clear from this plot that there is no obvious correlation between radio and X-ray fluxes. The majority of the radio-X-ray matches have a radio flux below 10 mJy. Three sources are detected below the radio flux density limit (1 mJy); two of these sources are optically star-like and X-ray bright sources of which one is spectroscopically identified as a QSO. The third source is an optically extended source and is spectroscopically identified as galaxy showing a narrow emission line. This source is classified as an AGN-2 based on its X-ray luminosity and hardness ratio. The lower panel in Figure 11 shows the full X-ray luminosity versus the radio luminosity, galaxies extend to lower radio/X-ray luminosities from the quasar population with some overlap. The majority of the radio-X-ray matches tend to have a small radio to X-ray luminosities ratios, corresponding to radio-quiet AGN. The small sample size and incompleteness of the spectroscopy do not allow more quantitative conclusions.

8 X-RAY-TO-OPTICAL FLUX RATIO

The X-ray to optical flux ratio is an important tool that can be used to explore the nature of the X-ray sources. Previous studies (e.g. Maccacaro et al. 1988; Elvis et al. 1994) have shown that there is an empirical relationship between X-ray and optical emission in AGN, and this can yield important information on the nature of AGN activity. In the X-ray optical plane, powerful unobscured AGNs (e.g. Stocke et al. 1991; Barger et al. 2003) typically have flux ratios of $-1 < \log f_{(2-7)\text{keV}}/f_{\text{opt}} < +1$, while star forming galaxies and low luminosity AGNs tend to have $\log f_{(2-7)\text{keV}}/f_{\text{opt}} \leq -1$ (e.g. Hornschemeier et al. 2001; Giacconi et al. 2002; Alexander et al. 2001). The X-ray-to-optical flux ratio is estimated from the relation (Hornschemeier et al. 2001):

$$\log \frac{f_X}{f_{\text{opt}}} = \log f_X + 0.4 R + 5.53, \quad (9)$$

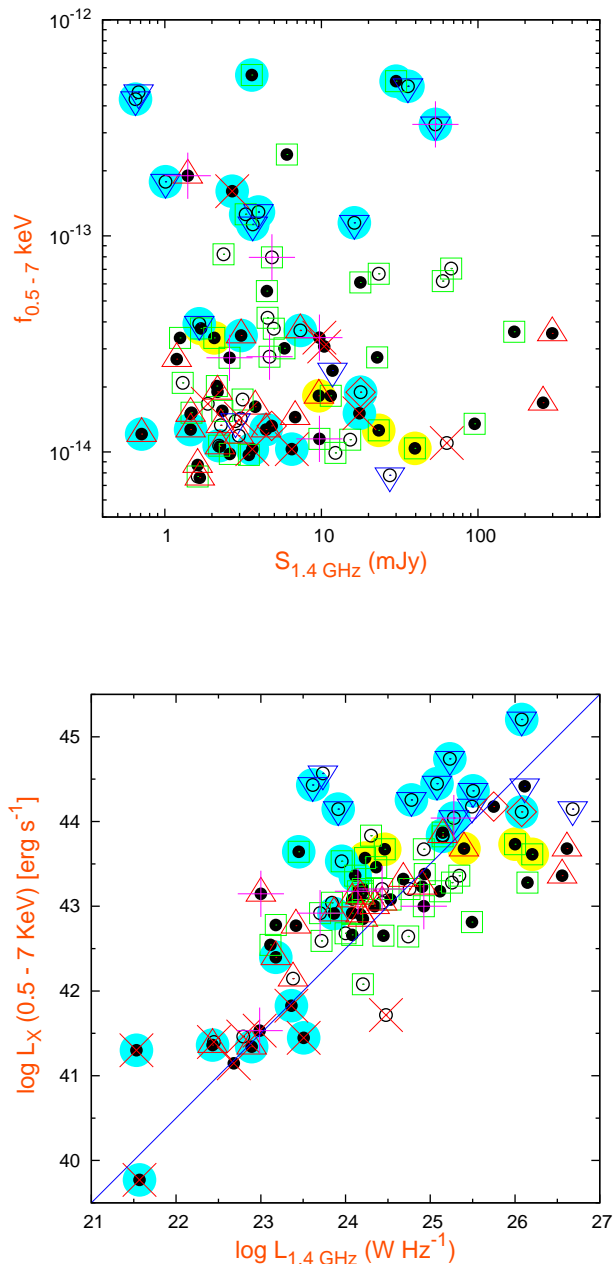


Figure 11. The upper panel shows the full X-ray flux/radio flux density distribution with the class of source indicated by the symbol. The lower panel displays the full X-ray luminosity versus the radio luminosity for the radio-X-ray matches. The symbols are the same as in Fig. 9.

where the flux is measured in units of $10^{-15} \text{ erg s}^{-1} \text{ cm}^{-2}$ in the considered X-ray band and R is the apparent R -band Vega magnitude.

Figure 12 plots the R magnitude as a function of the $0.5 - 7 \text{ keV}$ X-ray flux for the radio-X-ray matches (top panel). The middle panel displays the $2 - 7 \text{ keV}$ X-ray flux for the radio-X-ray matches. The filled diamonds illustrate the Akiyama et al. (2000) ASCA Large Sky Survey data (two clusters and one source without optical identifications have been excluded). The bottom panel shows the $0.5 - 2 \text{ keV}$ soft X-ray flux for the radio-X-ray

matches. The figures show that there is a large fraction of the sources that span the typical X-ray-to-optical flux ratio of the AGN region. The majority of the radio-X-ray matches (68%) fall within $\log f_{(2-7)\text{keV}}/f_{\text{opt}} = 0.0 \pm 1.0$. One notes that there is also a significant population ($\sim 23\%$) of sources that are X-ray over-luminous for their optical magnitudes [$\log f_{(2-7)\text{keV}}/f_{\text{opt}} > 1$], suggesting high redshift sources and/or dust obscuration (Alexander et al. 2001; Fiore et al. 2003; Brusa et al. 2004; Georgantopoulos et al. 2004; Mignoli et al. 2004; Gandhi et al. 2004; Georgakakis, et al. 2004). Among the sources with a high X-ray-to-optical flux ratio, five are EROs shown with large yellow filled circles. Two optically non-identified sources fit within this category but are not plotted here.

Recent studies have revealed a population of optically bright X-ray faint sources. Such a population was unveiled by the Chandra deep survey (Hornschemeier et al. 2001; Tozzi et al. 2001) and appear to be at $z \lesssim 1$. These sources appear mainly at very faint X-ray fluxes ($\lesssim 10^{-15} \text{ erg s}^{-1} \text{ cm}^{-2}$), and were found to comprise star-forming galaxies, normal galaxies and low luminosity AGN (with $L_X < 10^{42} \text{ erg s}^{-1}$ in the $0.5 - 10 \text{ keV}$ band). However, in this analysis 7 (8%) radio-X-ray matches are found to be optically bright-X-ray faint [$\log f_{(2-7)\text{keV}}/f_{\text{opt}} < -1$]. All are extended objects in the R band image (sources # 20, # 29, #39, # 42, # 44, # 48, # 71) and their R magnitude is in the range $15 < R < 18$ (and $I < 17$). Four of these sources are classified spectroscopically as galaxies: source # 29, source # 39, source # 42 and source #71, with spectroscopic redshifts of $z = 0.128$, $z = 0.126$, $z = 0.238$ and $z = 0.129$ respectively (see their spectra in Figure 19). Thus, these sources should be nearby, bright normal galaxies (see e.g. Barger et al. 2001; Tozzi et al. 2001; Hornschemeier et al. 2001). In addition, two sources (# 29 and # 39) of the spectroscopically identified sources are classified as AGN-2 (based on the X-ray luminosity) with $L_X[0.5 - 7 \text{ keV}] = 2.3 \times 10^{41} \text{ erg s}^{-1}$, and $L_X[0.5 - 7 \text{ keV}] = 2.2 \times 10^{41} \text{ erg s}^{-1}$ respectively. The two sources are classified as LINERS using the BPT diagram. So it is interesting that the two classification methods, optical and X-ray, are in good agreement. The other two sources (# 42 and # 71) are classified as normal galaxies based on their X-ray luminosity and classified as star-forming galaxies using the optical classification. Their X-ray luminosity are: $L_X[0.5 - 7 \text{ keV}] = 6.7 \times 10^{41} \text{ erg s}^{-1}$, and $L_X[0.5 - 7 \text{ keV}] = 2.8 \times 10^{41} \text{ erg s}^{-1}$ respectively.

8.1 Extremely red objects

Figure 13 shows the $R - K$ colour of the optical counterparts to the radio-X-ray matches as a function of the R magnitude. One notes that the $R - K$ colour tend to increase to fainter magnitudes. A Similar trend has been reported by several studies (e.g. Lehmann et al. 2001; Alexander et al. 2001; Mainieri et al. 2002). Galaxies (stellarity < 0.7) rapidly become redder than point-like objects (stellarity ≥ 0.7). One also notes the clear separation between the two groups. This can be seen in a more pronounced way in figure 17, where the $B_w - I$ colour is plotted versus the $I - K$ colour. The optical point sources tend to occupy a different region from the optically extended ones in the colour-colour diagram. The blue colour of point-like objects is consistent with those of quasars. Five interesting objects are associated with bright near infrared sources with $17 < K < 19$ and have colours $R - K > 5$ that would classify them as Extremely Red objects (EROs). In this subsample of the EROs, four are classified as AGN1 and one source is classified as AGN2 based on their X-ray properties. The red colour of the radio-X-ray matches can be explained by either obscured AGN or a high red-

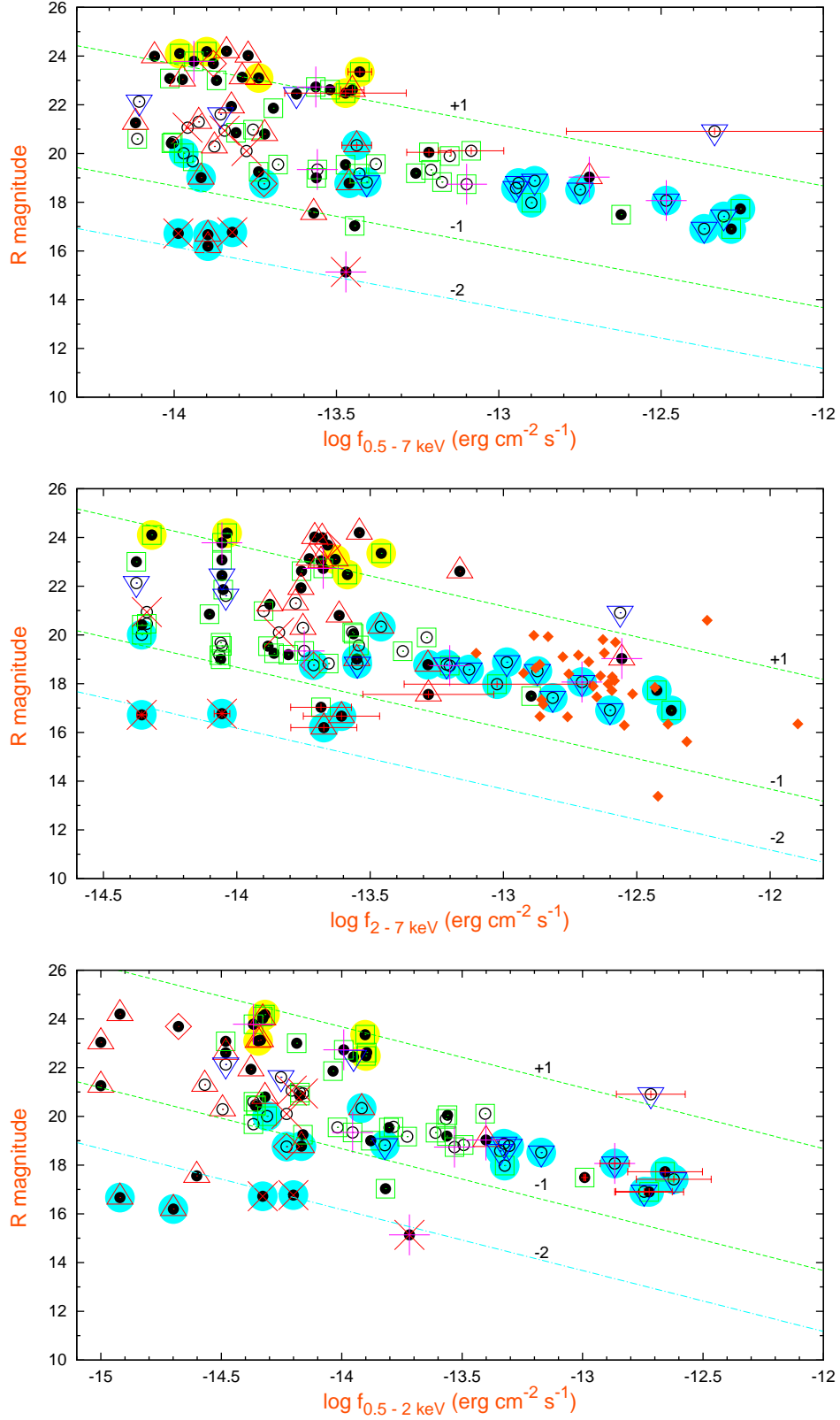


Figure 12. Optical R -band magnitude of the radio-X-ray matches plotted against the full (0.5-7 keV) X-ray fluxes in the top panel, hard (2-7 keV) X-ray fluxes in the middle panel and soft (0.5-2 keV) X-ray fluxes in the lower panel. The filled diamonds in the middle panel correspond to the sources in Akiyama et al. (2000). The solid lines denote the location of constant X-ray-to-optical flux ratios of $\log f_X/f_{opt}=1, 0, -1$ from top to bottom as given by equation 9. Same symbols as for the radio-X-ray matches in Fig 9.

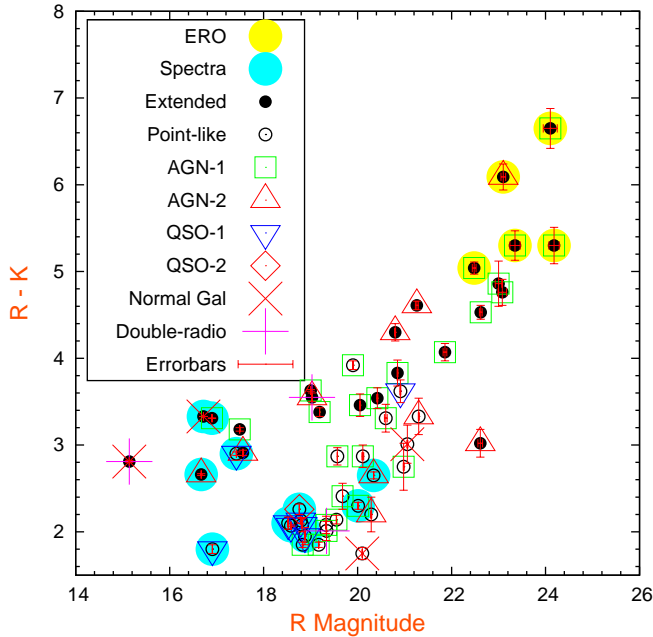


Figure 13. Colour magnitude diagram $R - K$ versus R -band magnitude for all radio-X-ray matches identified in both R and K bands in Boötes field.

shift cluster of galaxies (Lehmann et al. 2001). The extremely red colour of X-ray sources can be used as a good tracer of red galaxies at high redshifts. Near infrared spectroscopy observations have confirmed this (e.g. Cowie et al. 2001).

The ERO population is well known to be a mixture of old passively evolving elliptical and star-forming galaxies strongly reddened by dust extinction at high redshift ($z > 1$). Photometric and spectroscopic classifications (see e.g. Cimatti et al. 2003; Smail et al. 2002) have shown that the ERO population is almost equally divided between the two components.

The photometric redshift of the five EROs ranges from 0.88 to 1.77 and the spectral type classifies two EROs as ellipticals, two as starburst galaxies and the last one as lenticular. Moreover, these sources have a high X-ray to optical flux ratio $\log(f_x/f_{opt}) > 1$ (see Figure 14, yellow filled circles) and this signature can be used to identify high redshift X-ray sources. Obviously spectroscopic confirmation is required to explore this further. The X-ray luminosities in the 0.5-7 keV rest-frame energy band of the EROs are in the range $10^{43} - 10^{44}$ erg s^{-1} , suggesting that the EROs X-ray emission is most likely powered by AGN activity.

9 GENERAL PROPERTIES OF THE RADIO-X-RAY SAMPLE

9.1 HR-X-ray-to-optical flux ratio-colour

Figure 14 displays the X-ray-to-optical flux ratio (calculated using equation 9) as a function of the hardness ratio (upper panel) and as a function of the $B_w - R$ colour (lower panel). Although the radio-X-ray matches span a large range of hardness ratios, most sources cluster around the soft values ($HR \sim -0.4$). The majority of these sources have point-like optical morphology and 12 of them are spectroscopically identified as QSOs with broad emission lines and high f_x/f_{opt} , while two sources are spectroscopically identi-

fied as galaxies showing narrow emission lines with high X-ray-to-optical flux ratio ($\log f_x/f_{opt} > -1$) with high hardness ratio, possibly suggesting high column densities. The lower panel in Figure 14 shows that BLAGNs have bluer colour compared to not BLAGNs. The same figure shows that the optically extended sources have, on average, a red colour ($B_w - R \geq 1.5$), suggesting that the optical light is dominated by the host galaxy rather than the central AGN (e.g. Barger et al. 2003; Gandhi et al. 2004). Additional evidence that the optical/NIR light in many sources is dominated by the host galaxy can be seen in Figure 15 where the optical-NIR colour is plotted versus redshift and the magnitude respectively. Figure 15 displays the $R - K$ colour as a function of redshift. Overlaid are the optical/NIR colours of a QSO spectrum (Cristiani & Vio 1990; Cristiani et al. 2004) obtained from the template SED of the LEPHARE software and the mean observed spectra of three different galaxy types (E/S0, Sbc, Scd). Broad line AGNs, most of which exhibit soft X-ray spectra, have colours consistent with the QSO template prediction, while the extended sources follow the galaxy tracks. Again this figure illustrates an interesting segregation between optically extended and point-like objects, and clearly shows that optically extended objects have a redder colour while point-like objects tend to have a blue colour consistent with QSOs.

Figure 16 illustrates the hardness ratio as function of redshift (top panel) and the optical/near-infrared colour (bottom panel). This figure shows an interesting evolution of the hardness ratio with redshift of the radio-X-ray matches. The hardness ratio declines with redshift, and the majority of the hard X-ray counterparts to FIRST radio sources are at redshift lower than 1.5. This could be due to a combination of two effects. First, the fraction of AGN which are obscured is higher at lower luminosities (equals lower redshifts in a flux-limited sample). Second, the k -correction for obscured AGN pushes the less obscuration sensitive hard X-rays into the observed band at higher redshift. The hardness ratio versus $R - K$ optical colour is presented in the lower panel of Figure 16. In this diagram, no clear correlation between the hardness ratio and optical colour is observed. Ignoring the QSOs, it could be noted that the very hard sources all have low $R - K$. This is a consequence of the correlation of hardness ratio with redshift in Figure 16 (upper panel) and the fact that low $R - K$ galaxies are mostly at low redshift. One should note, however, that, in general, sources optically classified as obscured AGN are redder than unobscured AGN and also tend to have higher values of HR.

9.2 Colour-colour diagram

Figure 17 displays the $B_w - I$ colour versus the $I - K$ colour. The optical point sources tend to occupy a different region from the optically extended ones in the colour-colour diagram. The clear separation between the two groups reflects the effectiveness of the SExtractor parameter to separate extended objects (galaxies) and point-like objects (stars or QSOs). The blue colour of optical point-like objects is consistent with those of quasars. In addition to the point-like objects (13 sources) spectroscopically classified as quasars (cyan filled circles), 20 of the identifications have stellar optical profiles and all of these lie in the AGN region of the X-ray optical plane (see Figure 12), suggesting that they are QSOs rather than stars. Figure 18 shows the $B_w - R$ colour as a function of R magnitude. A similar trend is shown in this Figure. In this Figure a group of optically extended objects tend to have a bluer colour ($B_w - R < 1$) at fainter magnitudes ($22 < R < 24$). Akiyama et al. (2000) used this criterion to select candidates of BLAGNs in the LSS area.

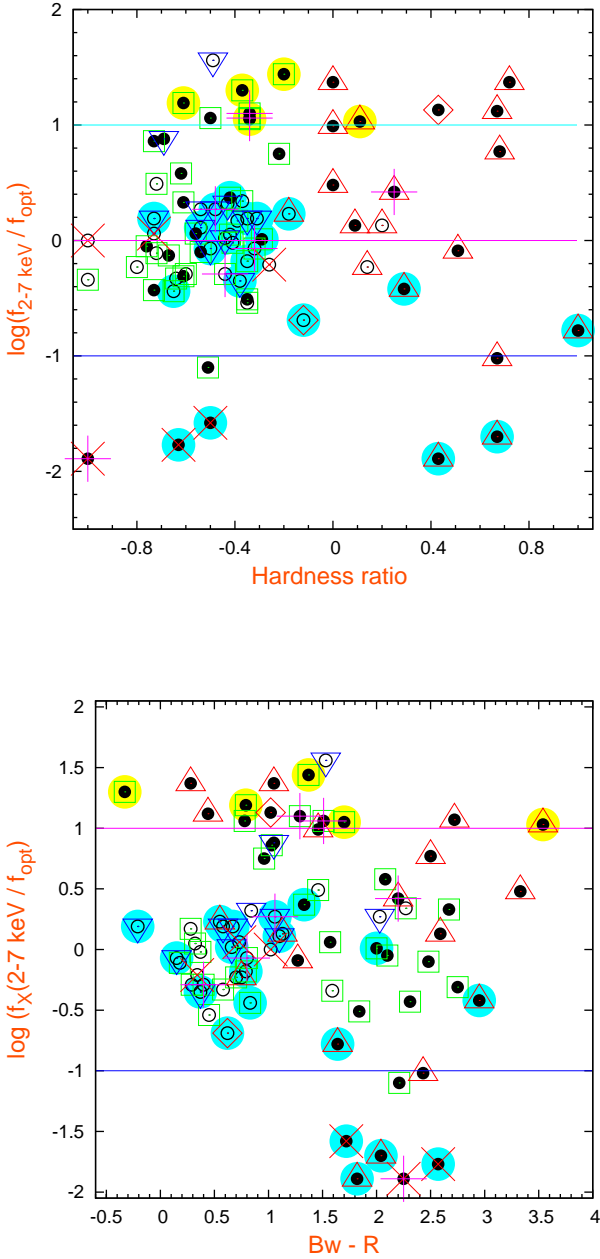


Figure 14. The X-ray-to-optical flux ratio as a function of the Hardness ratio HR (HR is defined as $(h-s)/(h+s)$ where h and s are the count rates in the 0.5 keV and 2–7 keV bands respectively) (top panel) and as a function of the optical colour $Bw - R$ (bottom panel). Horizontal lines show location of constant X-ray-to-optical flux ratio of +1, 0, and -1. Same symbols as for the radio-X-ray matches in Fig 9.

10 FINAL DATA TABLE

The final characteristics of the radio-X-ray matches are presented in Table 1, the table contains the following information:

- (1) source ID number;
- (2) X-ray object name (X-ray counterparts to FIRST radio sources);

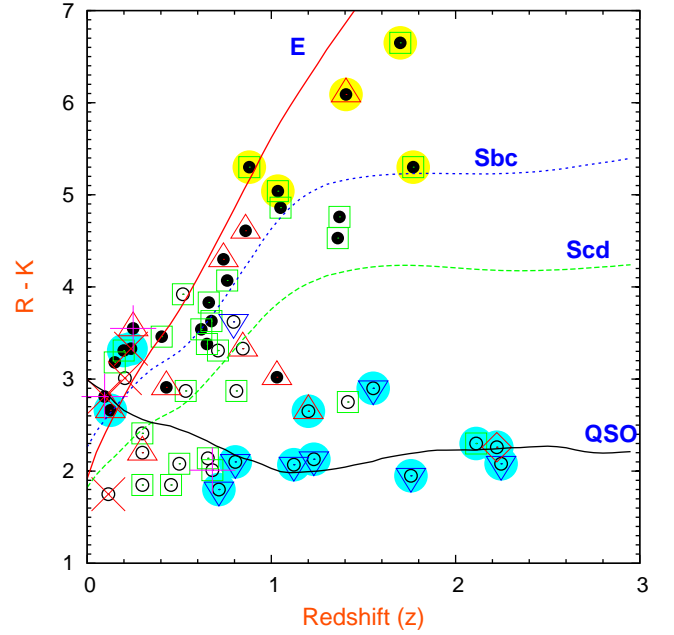


Figure 15. Optical/near-infrared colours as a function of photometric/spectroscopic redshift for the radio-X-ray matches. Same symbols as for the radio-X-ray matches in Fig9. The curves are different template SEDs for E/S0 (continuous), Sbc(dotted), Scd(dashed) and QSOs (black continuous). The galaxy templates are observed SEDs from ?. The QSO template is obtained from the set of QSOs SEDs of the LE PHARE software.

- (3)-(4) radio coordinates in hours, minutes and seconds;
- (5) radio flux in mJy;
- (6)-(7)-(8) the X-ray flux in the full (0.5-7) keV, soft (0.5-2) keV and hard (2-7) keV bands in units of $\text{erg s}^{-1} \text{cm}^{-2}$;
- (9) the hardness ratio HR, derived from the 0.5-2 and 2-8 keV band counts (Kenter et al. 2005);
- (10) X-ray-to-optical flux ratio;
- (11)-(12) log of X-ray luminosity in 0.5-2 keV, 2-7 keV and 0.5-7 keV respectively in erg s^{-1} ;
- (13) log of X-ray luminosity in 0.5-7 keV in erg s^{-1} ;
- (14) log of 1.4 GHz luminosity in W Hz^{-1} ;
- (15)-(16) the apparent R band magnitude associated with the corresponding errors and the $R - K$ colour respectively;
- (17) the source extractor stellarity parameter used to classify sources into point-like objects and extended sources;
- (18) the photometric redshift as derived from Hyperz with the corresponding errors. Sources with spectroscopic redshift are printed in bold face;
- (19) Classification obtained from the X-ray characteristics (based on the X-ray luminosity and the hardness ratio HR).

11 CONCLUSIONS

In this paper I have presented the broad band properties of a sample of 79 radio emitting X-ray sources, obtained from a correlation of the FIRST 1.4 GHz survey and the publicly available X-ray data of the medium depth XBoötes field. Out of ~ 900 FIRST radio sources that lie in the Boötes field, 92 have an X-ray counterparts

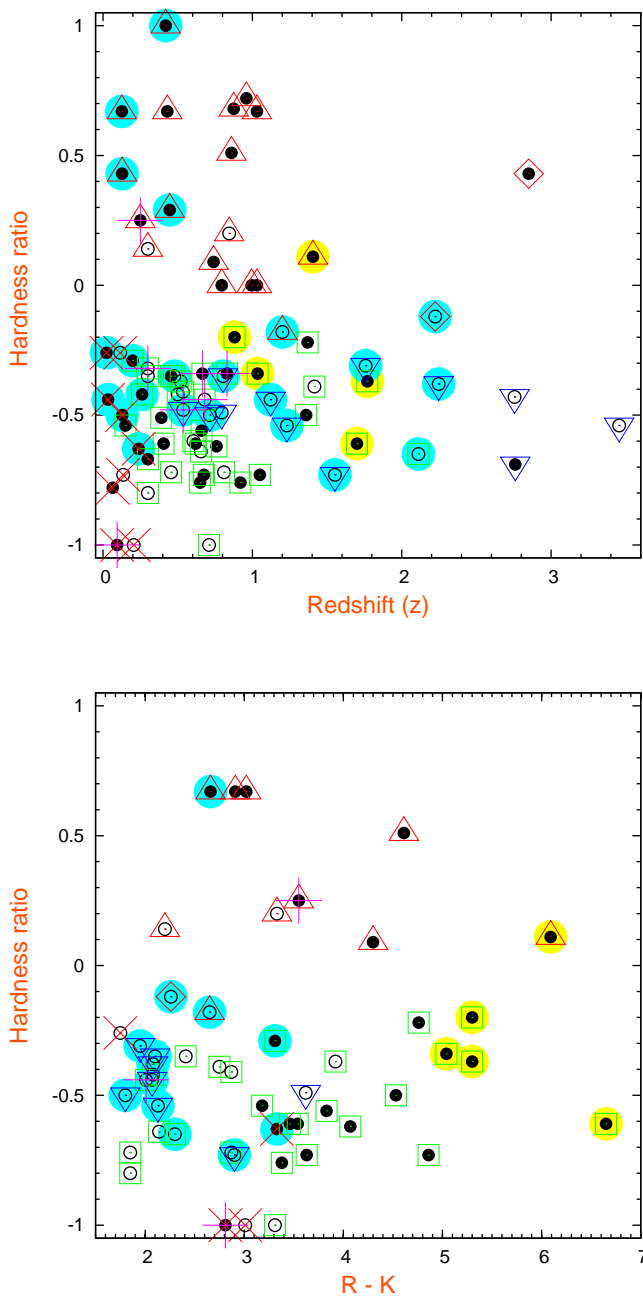


Figure 16. The hardness ratio as function of redshift is plotted in the top panel, and as a function of the optical/near-infrared colour is plotted in the bottom panel. Same symbols as for the radio-X-ray matches in Fig 9. A clear correlation between HR and the optical/near-infrared colour is not observed.

and 79 optical/infrareds sources are common to both radio and X-ray sources. All the 79 sources are identified in the full X-ray band (0.5-7 keV), 76 in the hard X-ray band (2-7 keV) and 77 in the soft band (0.5-2 keV). The main conclusions can be summarised as follows:

Optical spectra were obtained from the SDSS for 22 radio-X-ray matches. The majority of the spectroscopically identified sources are BL AGNs, 18% are classified as LINERs, 14% as

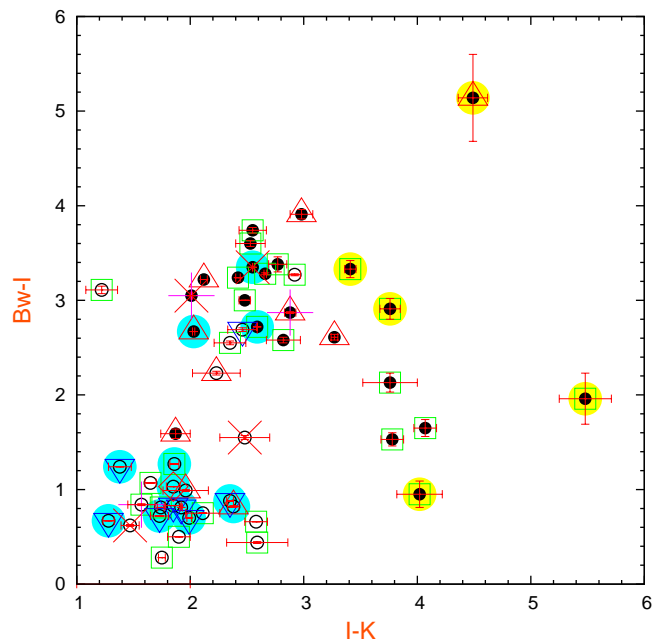


Figure 17. Colour-colour diagram for all radio-X-ray matches identified in B_w , I and K bands in Boötes field. Same symbols as for the radio-X-ray matches in Fig 9.

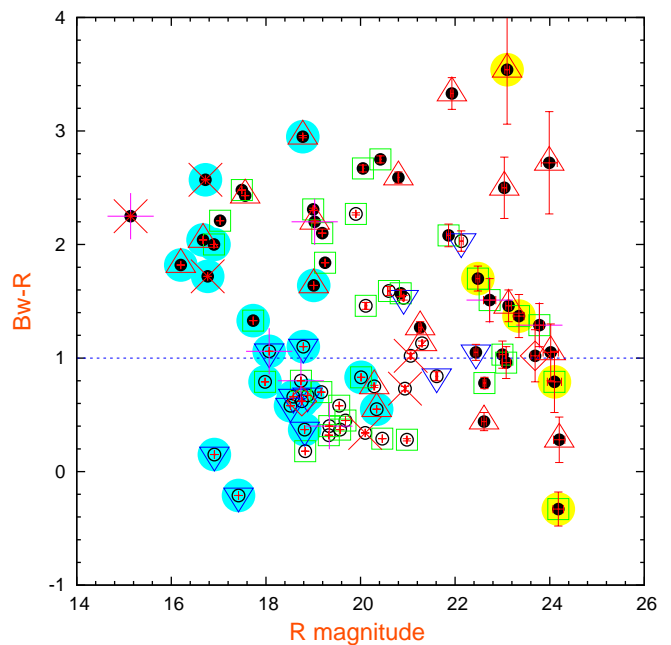


Figure 18. Colour magnitude diagram $B_w - R$ versus R -band magnitude for all radio-X-ray matches identified in both B_w and R bands in Boötes field. The horizontal line corresponds to $B_w - R = 1$. Same symbols as for the radio-X-ray matches in Fig 9.

star-forming galaxies and one source classified as BL Lac object. Among the sources with no spectroscopic classification 19 are point-like with blue colours and are most probably QSOs.

Photometric redshifts were calculated using the public code *Hyperz*. The redshift distribution of the AGNs shows a peak at $z \sim 0.7$, supporting previous studies (Barger et al. 2003) that show that the peak formation of super-massive black holes occurred at relatively recent times ($z < 1$). This leads to the conclusion that medium depth X-ray surveys are well suited for studying and probing this epoch effectively. Photometric redshifts were also used to investigate the $K - z$ relation. It is found that the $K - z$ relation obtained using photometric redshifts is similar to that obtained for brighter sources investigated by Willott et al. (2003) and Brookes et al. (2006). One should note that the K band catalogue is not as deep compared to the study of Willott et al. (2003). Deep K band data and more use of spectroscopic redshifts is required before strong conclusions can be drawn.

X-ray luminosities have been calculated using photometric redshifts and also spectroscopic redshift wherever available. The majority (88%) of the sources have a high X-ray luminosity in the full band, $L_X > 10^{42}$ erg s⁻¹, and 11% of sources have low X-ray luminosity, $L_X < 10^{42}$ erg s⁻¹. The classification of the radio-X-ray matches based on the hardness ratio and X-ray luminosity yielded 46% AGN-1 (unobscured), 24% AGN-2 (obscured), 15% QSO-1, 3% QSO-2 and 11% normal galaxies. One should note that 13 sources were spectroscopically classified as QSO (by SDSS) and 12/13 were classified as QSO-1 based on X-ray luminosity and hardness ratio. So it is interesting that the X-ray classification scheme is largely coincident with the classical AGN classification based on optical spectroscopic diagnostics.

The X-ray-to-optical flux ratios is a good discriminator between X-ray sources classes down to very faint optical magnitudes and X-ray fluxes, with AGN typically falling within the region defined by the loci $\log f_X/f_{opt} = 0 \pm 1$, and star-forming galaxies and low luminosity AGNs have $\log f_X/f_{opt} \leq -1$. The majority of the radio-X-ray matches (68%) are AGN ($\log f_X/f_{opt} = 0 \pm 1$). One notes again that all the sources classified as QSO (by SDSS) fall within this region. A significant population (23%) exists with high X-ray-to-optical flux ratio ($\log f_X/f_{opt} > 1$) corresponding to high redshift or dust obscuration, and 8% have low X-ray-to-optical flux ratio ($\log f_X/f_{opt} \leq -1$) that comprise normal galaxies and low X-ray luminosity sources.

The $R - K$ colour of the radio-X-ray matches get redder towards fainter R magnitudes, such trend is not present between $R - K$ and the K magnitude. Five radio-X-ray matches fall in the class of Extremely Red Objects, $R - K > 5$, with $17 < K < 19$. The majority (4/5) of the EROs tend to have soft X-ray hardness ratio, but the small sample size of the EROs and incompleteness of the infrared data do not allow for more conclusions.

Comparing the $R - K$ colours of the radio-X-ray matches with evolutionary tracks of various galaxy types and a QSO template as a function of redshift, I found that broad line AGNs, most of which exhibit soft X-ray spectra, have colours consistent with the QSO template prediction, while the extended objects follow the galaxy tracks indicating that these sources have colours dominated by the host galaxy.

No clear correlation found between the hardness ratio and optical/infrared colours. It is noted that the very hard sources tend to have low $R - K$ colour. This is a consequence of the correlation of the hardness ratio with redshift (see lower panel of figure 16) and the fact that low $R - K$ galaxies are mostly at low redshift. One should note, however, that, in general, sources optically classified

as obscured AGN are redder than unobscured AGN and also have higher values of hardness ratio.

Results from this study will be used to calculate the X-ray luminosity function and determine its evolution with redshift in a future study.

ACKNOWLEDGMENTS

I am very grateful to the referee Prof Simon Morris for the constructive and insightful suggestions. I would like to thank Dr Matt Jarvis and Prof Chris Willott for kindly supplying the stellar evolution curves. I would like to thank Dr Matt Hilton for providing me with a code to calculate the stellar evolutionary tracks. Thanks are also due to Prof Fethi Ahmed, Dr Kavilan Moodley and Dr Matt Hilton for proof reading this manuscript. The funding of my Ph.D by the South African Square Kilometer Array (SKA) project is greatly appreciated.

This work makes use of images data products provided by the NOAO Deep Wide-Field Survey (Jannuzi and Dey 1999), which is supported by the National Optical Astronomy Observatory (NOAO). NOAO is operated by AURA, Inc., under a cooperative agreement with the National Science Foundation.

This work also makes use of data products from the FLAMEX survey. FLAMEX was designed and constructed by the infrared instrumentation group (PI: R. Elston) at the University of Florida, Department of Astronomy, with support from NSF grant AST97-31180 and Kitt Peak National Observatory.

REFERENCES

- Afonso J., KoeKemoer, A. Norris, R.P., Cram, L., 2006, AJ, 131, 1230
 Akiyama M. et al., 2000, ApJs, 532, 700
 Alexander D. M., Brandt W. N., Hornschemeier A. E., Garmire G. P., Schneider D. P., Bauer F. E., Griffiths R. E., 2001, AJ, 122, 2156
 Antonucci R.R.J., 1993, ARA&A, 31, 473
 Baldwin, J. A., Phillips, M. M., Terlevich, R., 1981, PASP, 93, 5
 Barger A. J., Cowie L. L., Mushotzky R.F., Richards E.A., 2001, AJ, 121, 662
 Barger A. J., Cowie L. L., Wang, W.-H., 2007, ApJ, 654, 764
 Barger A.J., Cowie L.L., Brandt W.N., Capak P., Garmire G.P., Hornschemeier A.E., Steffen, A.T., Wehner E.H., 2002, AJ, 124, 1839
 Barger A.J. et al., 2003, AJ, 126, 632
 Bauer F.E., Alexander D.M., Brandt W.N., Schneider D.P., Treister E., Hornschemeier A.E., Garmire G.P., 2004, AJ, 128, 2048
 Bauer F. E., Alexander D. M., Brandt W. N., Hornschemeier A. E., Vignali C., Garmire G. P., Schneider D. P., 2002, AJ, 124, 2351
 Becker R. H., White R. L., Helfand D. J., 1995, ApJ, 450, 559
 Bell E.F., 2003, ApJ, 586, 794
 Benitez N., 2000, ApJ, 536, 571
 Bertin E., Arnouts S., 1996, A&AS, 117, 393
 Bolzonella M., Miralles J.-M., Pello R., 2000, A&A, 363, 476
 Boyle B.J., McMahon R.G., Wilkes, B.J., Elvis M., 1995, MNRAS, 276, 315
 Boyle B. J., Staveley-Smith L., Shanks T., Georgantopoulos I., Stewart G. C., Griffiths R. E., 1995, The Observatory, 115, 10
 Brand K. et al., 2006, ApJ, 641, 140
 Brandt W.N et al., 2001, AJ, 122, 2810

- Brinkmann W., Laurent-Muehleisen S.A., Voges W., Siebert R.H., Becker R.H., Brotherton M.S., White R.L., Gregg M.D., 2000, *A & A*, 356, 445
- Brookes M. H., Best P. N., Rengelink R., Rootgering H. J. A., 2006, *MNRAS*, 366, 1265
- Brown M. J. I., Dey A., Jannuzi B. T., Lauer T. R., Tiede G. P., Mikles V. J., 2003, *ApJ*, 597, 225
- Brusa M. et al., 2004, *A&A*, 409, 65
- Bruzual A. G., Charlot S., 1993, *ApJ*, 405, 538
- Cilieggi P., Vignali C., Comastri A., Fiore F., La Franca F., Perola G.C., 2003, *MNRAS*, 342, 575
- Cilieggi P., Elvis M., Wilkes B.J., Boyle B.J., McMahon R.G., 1997, *MNRAS*, 284, 401
- Cimatti A., Daddi E., Mignoli M., et al., *A & A*, 381, L68
- Condon J. J., 1992, *ARA&A*, 30, 575
- Condon J. J., Anderson M. L., Helou G., 1991, *ApJ*, 376, 95
- Condon, J. J., 1984, *ApJ*, 287, 461
- Cowie L.L. et al., 2001, *ApJ*, 551, L9
- Cristiani S., Vio R., 1990, *A&A*, 227, 385
- Cristiani S. et al., 2004, *ApJ*, 600, L119.
- de Ruiter H. R. et al., 1997, *A & A*, 319, 7
- de Vries W. H., Morganti R., Röttgering H. J. A., Vermeulen R., van Breugel W., Rengelink R., Jarvis M. J., 2002, *AJ*, 123, 1784
- Elvis M., Wilkes B.J., McDowell J.C., Green R.F., Willner S.P., Oey M.S., Polomski E., Cutri C., 1994, *ApJs*, 95, 1
- Elston R. J. et al., 2006, *Apj*, 639, 816
- El Bouchefry, K., 2009, *Astronomische Nachrichten*, 330, 107
- El Bouchefry K., 2008, submitted to *Astron.Nach*
- El Bouchefry K., Cress, C. M., 2007, *Astronomische Nachrichten*, 328, 577
- Fabbiano G., 1989, *ARA & A*, 27, 87
- Fiore, F., et al., 2008, *ApJ*, 672, 94
- Fiore F. et al., 2003, *A&A*, 79, 90
- Franceschini A. et al., 2003, *MNRAS*, 343, 1181
- Jarvis, M. J., & Rawlings, S., 2004, *New Astronomy Review*, 48, 1173
- Gandhi P., Crawford C.S., Fabian A.C., Johnstone R.M., 2004, *MNRAS*, 348, 529
- Georgakakis A., Hopkins A.M., Afonso J., Sullivan M., Mobasher B., 2004, *MNRAS*, 354, 127
- Georgantopoulos I., Georgakakis A., Akylas A., Stewart G.C., Giannakis O., Shanks T., Kitsionas S., 2004, *MNRAS*, 352, 91
- Giacconi R. et al., 2002, *ApJ*, 139, 369
- Gioia I.M., Maccacaro T., Schild R.E., Wolter A., Stocke J.T., Morris S.L., Henry J.P., 1990, *ApJS*, 72, 567
- Gilli R. et al., 2003, *ApJ*, 592, 721
- Gonzalez A.H., Maccarone T.J., 2002, *ApJ*, 581, 155
- Grimm H.-J., Gilfanov M., Sunyaev R., 2003, *MNRAS*, 339, 793
- Haarsma D. B., Partridge R. B., Windhorst R. A., Richards E. A., 2000, *ApJ*, 544, 641
- Hamilton T.T., Helfand D.J., 1993, *ApJ*, 418, 55
- Hasinger G. et al., 1998, *A & A*, 365, L65
- Hornschemeier A.E. et al., 2003, *AJ*, 126, 575
- Hornschemeier A.E. et al., 2001, *AJ*, 554, 742
- Hopkins A. M., Connolly A. J., Haarsma D. B., Cram L. E., 2001, *AJ*, 122, 288
- Jarvis M. J., Rawlings S., Eales S., Blundell K. M., Bunker A. J., Croft S., McLure R. J., Willott C. J., 2001, *MNRAS*, 326, 1585
- Kauffmann, G., et al. 2003, *MNRAS*, 346, 1055
- Kenter A. et al., 2005, *ApJS*, 161, 1
- Kewley, L. J., Groves, B., Kauffmann, G., Heckman, T., 2006, *mnras*, 372, 961
- Lehmann I. et al., 2001, *A&A*, 371, 833
- Maccacaro T., Gioia I. M., Wolter A., Zamorani G., Stocke J. T., 1988, *ApJ*, 326, 680
- Madau P., 1995, *ApJ*, 441,18
- Magliocchetti M., Maddox S. J., Lahav O., Wall J. V., 1998, *MNRAS*, 300, 257
- Magorian J., et al., *Aj*, 115, 2285
- Mainieri V. et al., 2002, *A&A*, 393, 425
- Merloni A., Heinz S., di Matteo T., 2003, *MNRAS*, 345, 1057
- Mignoli M. et al., 2004, *A&A*, 418, 827
- Mobasher B. et al., 2004, *ApJ*, 600, L167
- Miller G.E., Scalo J.M., 1979, *ApJS*, 41, 513
- Moretti A., Campana S., Lazzati D., Tagliaferri G., 2003, *ApJ*, 588, 696
- Moran E. C., Lehnert M. D., Helfand D. J., 1999, *ApJ*, 526, 649
- Murray S. S. et al., 2005, *ApJs*, 161, 1
- Mushotzky R.F. et al., 2000, *arxiv/00023v1*
- Nandra K., Pounds K.A., 1994, *MNRAS*, 268, 405
- Norman C. et al., 2004, *AJ*, 607, 721
- Norman C. et al., 2002, *ApJ*, 571, 218
- Oort, M. J. A., 1987, Leiden: Rijksuniversiteit, 1987,
- Ranalli P., Comastri A., Setti G., 2003, *AAP*, 399, 39
- Roche N. D., Dunlop J., Almaini O., 2003, *MNRAS*, 346, 803
- Rosati P. et al., 2002, *ApJ*, 566, 667.
- Rovilos E., Georgakakis A., Georgantopoulos I., Afonso J., Koekemoer A.M., Mobasher B., Goudis, C. 2007, *A & A*, 466, 119
- Sanchez-Sutil J.R., Munoz-Arjonilla A.J., Marti J., Garrido J.L., Perez-Ramirez D., Luque-Escamilla P., 2006, *A & A*, 452, 739
- Shapley A., Fabbiano G., Eskridge P.B., 2001, *ApJS*, 137, 139
- Schmidt M. et al., 1998, *A & A*, 329, 495
- Simpson C. et al., 2006, *MNRAS*, 372, 741
- Smail I., Owen F. N., Morrison G. E., Keel W. C., Ivison R. J., Ledlow M. J., 2002, *ApJ*, 581, 844
- Stern D. et al. 2002a, *AJ*, 123, 2223
- Stern D. et al., 2002b, *ApJ*, 568, 71
- Stocke J.T., Morris S.L., Gioia I.M., Maccacaro T., Schild R., Wolter A., Fleming T.A, Henry J.P., 1991, *ApJ*, 76, 813
- Szokoly G.P. et al., 2004, *ApJs*, 155, 271
- Urry C.M., Padovani P., 1995, *PASP*, 107, 803
- Tozzi P. et al., 2009, *arxiv:0902.2930*
- Tozzi P. et al., *ApJ*, 2001, 562, 42
- Voges W. et al., 1999, *A&A*, 349, 389
- Wang J. et al., 2004, *AJ*, 127, 213
- Willott C.J., Rawlings S., Jarvis M.J., Blundell K.M., 2003, *MNRAS*, 339, 173
- Windhorst, R. A., Miley, G. K., Owen, F. N., Kron, R. G., & Koo, D. C., 1985, *ApJ*, 289, 494
- Worsley M.A., Fabian A.C., Barcons X., Mateos S., Hasinger G., Brunner H., 2004, *MNRAS*, 352, L28
- Zheng W. et al., 2004, *ApJS*, 155, 73

Table 1. Characterisation of Faint Radio Sources

IDs (1)	Object name (2)	Ra (3)	Dec (4)	$S_{1.4}$ (5)	flux (6)	sflux (7)	hflux (8)	HR (9)	$\log(f_X/f_{opt})$ (10)	$\log(L_X)$ (11)	$\log(L_X)$ (12)	$\log L_X(0.5 - 7)$ (13)	$\log L_{1.4 GHz}$ (14)	R (15)	R-K (16)	Class (17)	Photo-Z (18)	Class (X-ray) (19)
1	J142449.3+340944	14 : 24 : 49.3	34 : 09 : 44.7	4.53	4.18	1.64	2.87	-0.41 ^{+0.07}	-0.02	42.76	43.00	43.15	24.20	19.57 ± 0.00	2.87	0.86	0.535 ^{+0.584}	AGN-1
2	J142456.3+351659	14 : 24 : 56.5	35 : 16 : 59.9	9.71	1.15	0.43	0.88	-0.34 ^{+0.21}	1.10	42.57	42.88	43.00	24.92	23.78 ± 0.09	0.01	0.830 ^{+0.383}	AGN-1
3	J142507.3+323137	14 : 25 : 7.3	32 : 31 : 37.5	3.28	12.60	4.75	9.46	-0.35 ^{+0.02}	-0.18	43.11	43.41	43.53	23.95	17.98 ± 0.00	1.00	0.478 ± 0.000	AGN-1
4	J142516.5+345246	14 : 25 : 16.5	34 : 52 : 46.6	63.21	1.10	0.62	0.00	-1.00 ^{+0.00}	0.00	41.48	41.72	24.48	21.06 ± 0.01	3.01	0.97	0.205 ^{+0.585}	Gal
5	J142524.2+340936	14 : 25 : 24.2	34 : 09 : 35.7	15.29	1.14	0.43	0.87	-0.35 ^{+0.22}	-0.54	41.65	41.96	42.08	24.20	19.68 ± 0.00	2.41	0.98	0.300 ^{+0.000}	AGN-1
6	J142532.8+330125	14 : 25 : 32.8	33 : 01 : 25.4	7.33	3.65	1.21	3.47	-0.18 ^{+0.08}	0.23	43.36	43.82	43.84	25.15	20.34 ± 0.00	2.65	0.95	1.201 ± 0.001	AGN-2
7	J142533.5+345805	14 : 25 : 33.5	34 : 58 : 5.7	2.97	1.19	0.27	1.66	+0.20 ^{+0.28}	0.13	42.38	43.18	43.04	24.43	21.30 ± 0.01	3.33	0.98	0.845 ^{+0.883}	AGN-2
8	J142543.9+335534	14 : 25 : 43.9	33 : 55 : 33.2	298.44	3.54	0.33	6.86	+0.67 ^{+0.26}	1.12	42.65	43.97	43.68	26.61	22.61 ± 0.05	3.02	0.08	1.030 ^{+0.817}	AGN-2
9	J142552.6+340239	14 : 25 : 52.6	34 : 02 : 39.5	1.25	3.37	1.57	1.31	-0.67 ^{+0.08}	-0.13	42.20	42.15	42.54	23.11	19.54 ± 0.01	0.03	0.300 ^{+0.000}	AGN-1
10	J142601.8+343106	14 : 26 : 1.9	34 : 31 : 7.1	3.14	1.75	0.67	1.26	-0.39 ^{+0.08}	0.17	43.26	43.53	43.67	24.92	20.98 ± 0.01	2.75	0.98	1.415 ^{+0.000}	AGN-1
11	J142607.7+340425	14 : 26 : 7.7	34 : 04 : 26.3	35.70	49.30	23.90	15.30	-0.73 ^{+0.01}	0.19	44.89	44.70	45.20	26.08	17.42 ± 0.00	2.90	1.00	1.553 ± 0.001	QSO-1
12	J142611.1+334201	14 : 26 : 11.0	33 : 42 : 1.7	2.17	1.90	0.48	2.42	+0.09 ^{+0.16}	0.13	42.52	43.20	43.11	24.18	20.80 ± 0.01	4.30	0.03	0.740 ^{+0.760}	AGN-2
13	J142611.1+333932	14 : 26 : 11.1	33 : 39 : 32.7	1.70	3.73	1.25	3.48	-0.20 ^{+0.08}	1.44	43.08	43.53	43.57	24.23	23.35 ± 0.11	5.30	0.03	0.880 ^{+0.722}	AGN-1
14	J142620.3+353707	14 : 26 : 20.4	35 : 37 : 8.4	6.02	23.80	10.20	12.70	-0.54 ^{+0.01}	-0.10	42.41	42.51	42.78	23.18	17.49 ± 0.00	3.18	0.03	0.150 ^{+0.392}	AGN-1
15	J142624.2+334632	14 : 26 : 24.2	33 : 46 : 32.8	3.44	0.97	0.33	0.88	-0.22 ^{+0.01}	0.75	42.91	43.34	43.38	24.93	23.08 ± 0.09	4.76	0.08	1.370 ^{+0.086}	AGN-1
16	J142632.2+3350814	14 : 26 : 32.2	35 : 08 : 14.7	95.31	1.35	0.65	0.42	-0.73 ^{+0.16}	0.86	42.97	42.78	43.28	26.15	23.00 ± 0.07	4.86	0.27	1.050 ^{+1.156}	AGN-1
17	J142632.6+334621	14 : 26 : 32.4	33 : 46 : 21.3	1.67	0.76	0.10	1.33	+0.51 ^{+0.39}	-0.09	41.97	43.08	42.85	24.20	21.26 ± 0.03	4.61	0.03	0.860 ^{+0.987}	AGN-2
18	J142633.6+333211	14 : 26 : 33.6	33 : 32 : 11.8	4.97	3.72	1.87	0.86	-0.80 ^{+0.31}	-0.23	42.28	41.95	42.59	23.72	19.17 ± 0.00	1.85	0.99	0.300 ^{+0.795}	AGN-1
19	J142651.5+331924	14 : 26 : 51.5	35 : 19 : 24.7	3.96	12.90	4.72	10.30	-0.31 ^{+0.05}	0.19	44.30	44.64	44.74	25.23	18.88 ± 0.00	1.95	0.83	1.758 ± 0.002	QSO-1
20	J142659.6+341158	14 : 26 : 59.7	34 : 12 : 0.2	9.71	3.38	1.91	0.00	-1.00 ^{+0.00}	-1.89	41.28	41.53	22.99	15.14 ± 0.00	2.81	0.03	0.095 ^{+0.154}	Gal
21	J142708.6+331508	14 : 27 : 8.7	33 : 15 : 8.9	10.42	3.08	1.53	0.79	-0.78 ^{+0.07}	31.62	40.85	40.57	41.15	22.68	0.03	0.065 ^{+0.000}	Gal
22	J142731.4+324435	14 : 27 : 31.4	32 : 44 : 34.4	2.25	1.06	0.10	2.07	+0.68 ^{+0.25}	0.77	41.99	43.30	43.00	24.34	23.04 ± 0.05	0.02	0.875 ^{+0.932}	AGN-2
23	J142735.5+341927	14 : 27 : 35.6	34 : 19 : 28.1	2.59	2.73	1.02	2.11	-0.34 ^{+0.21}	1.06	42.75	43.04	43.18	24.15	22.73 ± 0.13	0.00	0.665 ^{+0.853}	AGN-1
24	J142741.4+325433	14 : 27 : 41.6	32 : 54 : 32.1	1.62	0.87	0.00	2.09	+1.10 ^{+0.65}	1.07	43.28	42.90	24.18	23.99 ± 0.17	0.04	0.855 ^{+1.051}	AGN-2
25	J142744.4+333828	14 : 27 : 44.4	33 : 38 : 28.6	16.24	11.50	4.96	6.12	-0.54 ^{+0.03}	0.11	44.00	44.08	44.36	25.51	18.79 ± 0.00	2.13	0.97	1.231 ± 0.001	QSO-1
26	J142750.4+344100	14 : 27 : 50.3	34 : 41 : 0.8	1.62	0.77	0.43	0.00	-1.00 ^{+0.00}	-0.34	42.43	42.68	24.00	20.60 ± 0.03	3.31	0.83	0.710 ^{+0.743}	AGN-1
27	J142752.2+335031	14 : 27 : 52.2	35 : 30 : 31.8	2.28	1.33	0.32	1.77	+0.14 ^{+0.19}	-0.23	41.52	42.26	42.15	23.38	20.29 ± 0.01	2.20	0.95	0.300 ^{+0.511}	AGN-2
28	J142810.3+353846	14 : 28 : 10.3	35 : 38 : 47.0	1.01	17.80	6.74	13.40	-0.35 ^{+0.19}	0.19	43.74	44.04	44.15	23.91	18.52 ± 0.00	2.10	0.97	0.804 ± 0.001	QSO-1
29	J142850.2+323248	14 : 28 : 50.3	32 : 32 : 48.8	1.46	1.27	0.20	2.12	+0.43 ^{+0.20}	-1.89	40.56	41.59	41.36	22.43	16.20 ± 0.00	0.03	0.128 ± 0.000	AGN-2
30	J142852.7+325026	14 : 28 : 52.7	32 : 50 : 27.2	3.07	3.46	0.68	5.21	+0.29 ^{+0.08}	-0.42	42.20	43.08	42.91	23.86	18.78 ± 0.00	0.03	0.446 ± 0.000	AGN-2
31	J142905.1+342640	14 : 29 : 5.1	34 : 26 : 41.1	260.41	1.69	0.47	1.96	+0.00 ^{+0.17}	1.37	42.81	43.43	43.36	26.56	24.02 ± 0.16	0.51	1.030 ^{+1.046}	AGN-2
32	J142910.2+352946	14 : 29 : 10.2	35 : 29 : 46.9	17.81	1.89	0.59	1.94	-0.12 ^{+0.15}	-0.69	43.61	44.11	44.11	26.08	18.76 ± 0.00	2.26	0.98	2.224 ± 0.001	QSO-2
33	J142911.1+350320	14 : 29 : 11.2	35 : 03 : 20.7	2.37	8.22	3.94	2.71	-0.72 ^{+0.04}	0.49	43.51	43.34	43.83	24.30	20.11 ± 0.02	2.87	1.00	0.810 ^{+0.822}	AGN-1
34	J142916.1+335536	14 : 29 : 16.1	33 : 55 : 38.8	2.07	3.37	1.26	2.60	-0.34 ^{+0.21}	1.05	43.23	43.56	43.67	24.46	22.48 ± 0.04	5.04	0.04	1.035 ^{+1.102}	AGN-1
35	J142917.4+332626	14 : 29 : 17.4	33 : 26 : 26.4	6.79	1.45	0.12	2.88	+0.72 ^{+0.21}	1.37	42.15	43.53	43.23	24.90	24.20 ± 0.12	0.11	0.960 ^{+1.257}	AGN-2
36	J142922.8+351218	14 : 29 : 22.8	35 : 12 : 19.7	1.48	1.52	0.74	0.43	-0.76 ^{+0.16}	31.31	42.90	42.66	43.20	24.20	0.00	0.50	0.920 ^{+0.806}	AGN-1
37	J142942.6+335654	14 : 29 : 42.6	33 : 56 : 55.0	3.64	11.30	4.55	7.43	-0.44 ^{+0.22}	0.02	43.87	44.08	44.26	24.78	18.58 ± 0.00	2.07	0.98	1.122 ± 0.001	QSO-1
38	J142955.6+353707	14 : 29 : 55.7	35 : 37 : 7.6	11.78	2.38	1.12	0.88	-0.69 ^{+0.12}	0.88	44.08	43.98	44.41	26.11	22.44 ± 0.04	0.35	2.760 ^{+3.001}	QSO-1
39	J143003.1+340649	14 : 30 : 3.1	34 : 06 : 51.3	4.43	1.27	0.12	2.47	+0.67 ^{+0.25}	-1.70	40.32	41.64	41.34	22.89	16.67 ± 0.00	2.66	0.31	0.126 ± 0.000	AGN-2
40	J143008.8+344713	14 : 30 : 8.9	34 : 47 : 13.8	27.38	0.78	0.33	0.42	-0.54 ^{+0.19}	0.27	43.76	43.87	44.15	26.68	22.13 ± 0.04	0.80	3.455 ^{+3.552}	QSO-1
41	J143011.5+350019	14 : 30 : 11.5	35 : 00 : 19.7	4.66	2.76	1.11	1.79	-0.44 ^{+0.10}	-0.29	42.80	43.00	43.20	24.43	19.34 ± 0.00	2.01	0.98	0.680 ^{+0.181}	AGN-1
42	J143103.6+334541	14 : 31 : 3.4	33 : 45 : 41.6	3.62	1.03	0.47	0.44	-0.63 ^{+0.23}	-1.77	41.48	41.45	41.83	23.36	16.72 ± 0.00	3.33	0.03	0.238 ± 0.000	Gal
43	J143112.4+335527	14 : 31 : 12.5	35 : 35 : 27.3	9.64	1.82	0.45	2.34	+0.11 ^{+0.15}	1.03	43.08	43.79	43.68	25.40	23.10 ± 0.05	6.09	0.27	1.405 ^{+1.447}	AGN-2
44	J143114.4+323225	14 : 31 : 14.3	32 : 32 : 25.6	170.73	3.60	1.52	2.07	-0.51 ^{+0.07}	-1.10	42.43	42.57	42.81	25.49	17.03 ± 0.00	0.03	0.390 ^{+1.044}	AGN-1
45	J143121.8+344046	14 : 31 : 21.9	34 : 40 : 46.6	1.40	19.00	3.97	27.80	+0.25 ^{+0.03}	0.42	42.45	43.30	43.15	23.00	19.03 ± 0.00	3.55	0.03	0.250 ^{+0.319}	AGN-2
46	J143125.0+331350	14 : 31 : 25.3	33 : 13 : 48.3	6.47	1.03	0.36	0.90	-0.26 ^{+0.28}	31.14	39.32	39.72	39.77	21.57	0.04	0.023 ± 0.000	Gal
47	J143127.7+343740	14 : 31 : 27.9	34 : 37 : 40.9	2.83	1.39	0.56	0.91	-0.43 ^{+0.20}	0.32	43.79	44.00	44.18	25.49	21.61 ± 0.02	0.98	2.755 ^{+2.902}	QSO-1
48	J143131.1+342721	14 : 31 : 31.1	34 : 27 : 22.1	1.19	2.69	0.25	5.23	+0.67 ^{+0.12}	-1.02	41.74	43.04	42.77	23.41	17.56 ± 0.00	2.91	0.03	0.430 ^{+0.417}	AGN-2
49	J143152.3+323213	14 : 31 : 52.3	32 : 32 : 13.4	4.83	7.96	2.94	6.29	-0.32 ^{+0.03}	-0.07	42.49	42.82	42.92	23.70	18.74 ± 0.00	0.97	0.300 ^{+0.357}	AGN-1
50	J143156.4+325137	14 : 31 : 56.4	32 : 51 : 37.8	0.71	1.21	0.00	2.82	+1.00 ^{+0.35}	-0.78	42.77	42.40	23.18	19.01 ± 0.00	0.40	0.420 ± 0.001	AGN-2
51	J143157.9+341649	14 : 31 : 57.9	34 : 16 : 50.3	0.65	42.90	18.00	25.10	-0.50 ^{+0.01}	-0.07	44.04	44.20	44.43	23.61	16.91 ± 0.00	1.80	0.99	0.715 ± 0.001	QSO-1

X-ray identification of FIRST

Table 1. *Continued...*

IDs	Object name	Ra	Dec	$S_{1.4}$ (mJy)	flux $\times 10^{-15}$	sflux ($\text{ergs}^{-1}\text{m}^{-2}$)	hflux	HR	$\log(f_X/f_{opt})$	$\log L_X$ (0.5-2) keV	$\log L_X$ (2-7) Kev	$\log L_X$ (0.5-7) Kev	$\log L_{1.4\text{ GHz}}$ (W Hz $^{-1}$)	R	R-K	Class	Photo-Z	Class (X-ray)
(1)	(2)	(3)	(4)	(5)	(6)	(7)	(8)	(9)	(10)	(11)	(12)	(13)	(14)	(15)	(16)	(17)	(18)	(19)
52	J143214.3+342605	14 : 32 : 14.3	34 : 26 : 5.7	17.75	6.09	2.75	2.74	-0.61 ^{+0.04} _{-0.04}	0.33	42.72	42.72	43.08	24.53	20.05 ± 0.01	3.46	0.03	0.405 ^{+0.505} _{-0.345}	AGN-1
53	J143308.1+353151	14 : 33 : 8.1	35 : 31 : 51.4	2.33	1.55	0.67	0.79	-0.56 ^{+0.14} _{-0.16}	0.06	42.56	42.62	42.92	24.08	20.85 ± 0.01	3.83	0.03	0.660 ^{+0.675} _{-0.582}	AGN-1
54	J143311.0+335828	14 : 33 : 11.1	33 : 58 : 28.8	22.72	2.74	1.32	0.87	-0.73 ^{+0.09} _{-0.10}	-0.43	42.87	42.69	43.18	25.11	19.00 ± 0.00	3.63	0.03	0.675 ^{+0.685} _{-0.647}	AGN-1
55	J143315.7+332858	14 : 33 : 15.7	33 : 28 : 58.4	5.81	3.02	1.27	1.75	-0.50 ^{+0.08} _{-0.09}	1.06	43.49	43.63	43.87	25.15	22.62 ± 0.03	4.53	0.52	1.360 ^{+1.348} _{-1.297}	AGN-1
56	J143318.5+344404	14 : 33 : 18.5	34 : 44 : 4.3	2.69	16.10	6.51	10.40	-0.44 ^{+0.02} _{-0.02}	32.34	40.91	41.11	41.30	21.53	0.03	0.034 ± 0.001	Gal
57	J143355.1+340933	14 : 33 : 55.2	34 : 09 : 34.3	3.06	1.43	0.69	0.46	-0.73 ^{+0.16} _{-0.22}	0.06	41.15	40.97	41.46	22.79	20.94 ± 0.01	0.98	0.135 ^{+0.236} _{+0.000}	AGN-1
58	J143413.9+345506	14 : 34 : 13.8	34 : 55 : 6.2	2.60	0.98	0.44	0.44	-0.61 ^{+0.23} _{-0.30}	-0.31	42.32	42.32	42.66	24.08	20.42 ± 0.01	3.54	0.03	0.620 ^{+0.640} _{-0.592}	AGN-1
59	J143423.3+342610	14 : 34 : 23.4	34 : 26 : 9.9	3.78	1.62	0.46	1.87	+0.00 ^{+0.17} _{-0.17}	0.99	42.76	43.38	43.32	24.68	23.13 ± 0.06	0.28	0.995 ^{+1.039} _{-0.870}	AGN-2
60	J143428.0+331102	14 : 34 : 28.0	33 : 11 : 2.0	23.23	1.26	0.48	0.92	-0.37 ^{+0.12} _{-0.24}	1.30	43.32	43.59	43.73	26.00	24.18 ± 0.11	5.30	0.22	1.770 ^{+1.802} _{-1.753}	AGN-1
61	J143434.2+351009	14 : 34 : 34.2	35 : 10 : 9.5	67.51	7.06	2.71	5.15	-0.37 ^{+0.04} _{-0.04}	0.34	42.94	43.23	43.36	25.34	19.90 ± 0.00	3.92	0.98	0.520 ^{+0.543} _{-0.449}	AGN-1
62	J143445.3+332820	14 : 34 : 45.3	33 : 28 : 20.6	30.03	52.00	18.90	42.60	-0.29 ^{+0.00} _{+0.00}	0.01	42.92	43.28	43.36	24.11	16.90 ± 0.00	3.31	0.01	0.198 ± 0.001	AGN-1
63	J143513.2+333117	14 : 35 : 13.3	33 : 31 : 18.3	2.15	2.02	0.92	0.89	-0.62 ^{+0.13} _{-0.15}	0.58	42.82	42.81	43.18	24.20	21.86 ± 0.04	4.07	0.04	0.760 ^{+0.782} _{-0.747}	AGN-1
64	J143527.3+331240	14 : 35 : 27.3	33 : 12 : 40.1	1.30	2.09	0.96	0.88	-0.64 ^{+0.11} _{-0.13}	-0.33	42.71	42.66	43.04	23.84	19.55 ± 0.00	2.14	0.98	0.655 ^{+0.701} _{-0.598}	AGN-1
65	J143527.9+350928	14 : 35 : 27.9	35 : 09 : 28.3	1.66	3.92	1.51	2.83	-0.38 ^{+0.07} _{-0.07}	-0.35	44.04	44.30	44.45	25.08	18.82 ± 0.00	2.08	0.99	2.247 ± 0.002	QSO-1
66	J143528.0+331145	14 : 35 : 28.0	33 : 11 : 45.5	39.60	1.04	0.47	0.48	-0.61 ^{+0.23} _{-0.29}	1.19	43.26	43.28	43.61	26.20	24.10 ± 0.15	6.65	0.09	1.700 ^{+1.802} _{-1.753}	AGN-1
67	J143528.4+331931	14 : 35 : 28.4	33 : 19 : 31.5	23.27	6.68	3.21	2.21	-0.72 ^{+0.04} _{-0.04}	-0.11	42.90	42.74	43.20	24.76	18.83 ± 0.00	1.85	0.99	0.455 ^{+0.529} _{-0.374}	AGN-1
68	J143541.6+345055	14 : 35 : 41.6	34 : 50 : 55.3	1.46	1.50	0.42	1.74	+0.00 ^{+0.17} _{-0.17}	0.48	42.52	43.15	43.08	24.08	21.93 ± 0.03	0.08	0.795 ^{+0.816} _{-0.781}	AGN-2
69	J143547.6+335310	14 : 35 : 47.6	33 : 53 : 9.9	2.22	1.07	0.49	0.44	-0.65 ^{+0.24} _{-0.31}	-0.44	43.48	43.43	43.83	25.15	20.01 ± 0.00	2.30	0.98	2.112 ± 0.001	AGN-1
70	J143608.7+350613	14 : 36 : 8.7	35 : 06 : 13.8	0.68	46.20	19.20	27.40	-0.49 ^{+0.01} _{-0.01}	1.56	44.18	44.34	44.57	23.73	20.91 ± 0.01	3.62	0.79	0.795 ^{+0.819} _{-0.779}	QSO-1
71	J143623.4+352710	14 : 36 : 23.4	35 : 27 : 10.8	17.48	1.51	0.63	0.88	-0.50 ^{+0.16} _{-0.18}	-1.58	41.08	41.20	41.45	23.51	16.77 ± 0.00	0.03	0.129 ± 0.000	Gal
72	J143644.2+350626	14 : 36 : 44.2	35 : 06 : 27.1	4.81	1.32	0.21	2.19	+0.43 ^{+0.20} _{-0.18}	1.13	43.40	44.41	44.18	25.75	23.69 ± 0.09	0.00	2.850 ^{+3.284} _{-1.916}	QSO-2
73	J143651.3+333909	14 : 36 : 51.3	33 : 39 : 10.2	1.88	1.67	0.59	1.44	-0.26 ^{+0.17} _{-0.18}	-0.21	40.94	41.32	41.40	22.45	20.10 ± 0.00	1.75	0.99	0.115 ^{+0.143} _{+0.000}	Gal
74	J143713.5+350553	14 : 37 : 13.6	35 : 05 : 54.8	59.62	6.18	2.45	4.19	-0.42 ^{+0.05} _{-0.05}	0.05	42.87	43.11	43.28	25.26	19.33 ± 0.00	2.08	0.99	0.500 ^{+0.557} _{-0.206}	AGN-1
75	J143715.3+340652	14 : 37 : 15.3	34 : 06 : 52.5	4.48	5.55	2.73	1.56	-0.76 ^{+0.04} _{-0.04}	-0.05	43.15	42.91	43.46	24.36	19.19 ± 0.00	3.38	0.06	0.650 ^{+0.660} _{-0.634}	AGN-1
76	J143752.0+351939	14 : 37 : 52.0	35 : 19 : 40.1	11.48	1.82	0.69	1.38	-0.35 ^{+0.15} _{-0.16}	-0.51	42.23	42.53	42.65	24.45	19.25 ± 0.00	0.03	0.455 ^{+0.469} _{-0.443}	AGN-1
77	J143756.4+351936	14 : 37 : 56.5	35 : 19 : 36.5	53.48	32.80	13.60	19.70	-0.48 ^{+0.01} _{-0.01}	0.27	43.67	43.84	44.04	25.28	18.07 ± 0.00	0.74	0.537 ± 0.01	QSO-1
78	J143821.8+344000	14 : 38 : 21.8	34 : 40 : 1.1	12.28	0.99	0.44	0.46	-0.60 ^{+0.29} _{-0.29}	-0.29	42.30	42.32	42.64	24.74	20.46 ± 0.00	0.98	0.605 ^{+0.727} _{-0.499}	AGN-1
79	J143830.2+353915	14 : 38 : 30.2	35 : 39 : 15.9	3.59	55.50	22.00	37.60	-0.42 ^{+0.01} _{-0.01}	0.37	43.23	43.48	43.64	23.45	17.73 ± 0.00	0.03	0.262 ± 0.001	AGN-1

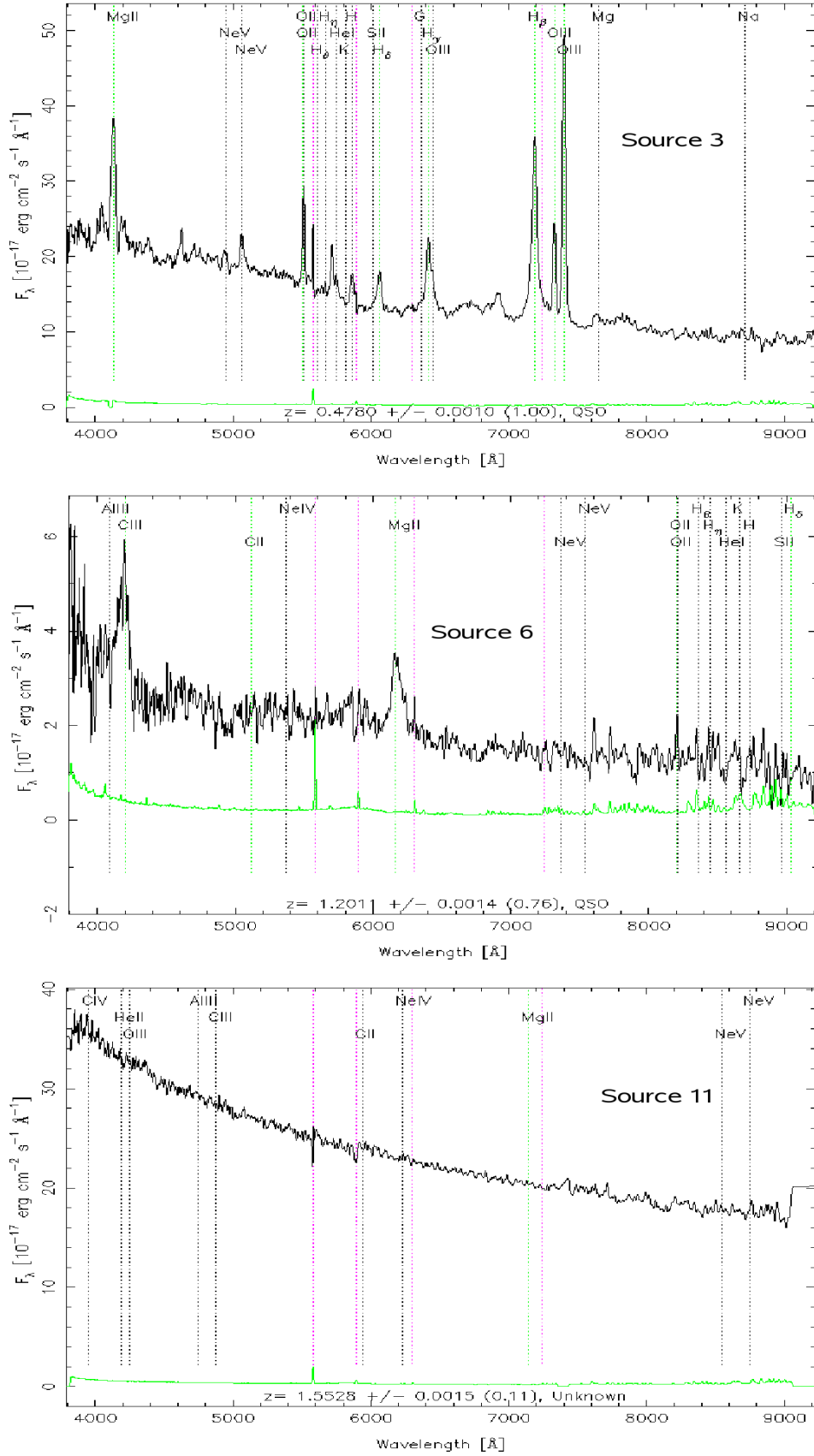


Figure 19. Optical spectra of 22 radio-X-ray matches obtained from the SDSS survey. The spectrum of each object is shown with the identification label, spectroscopic redshift and classification.

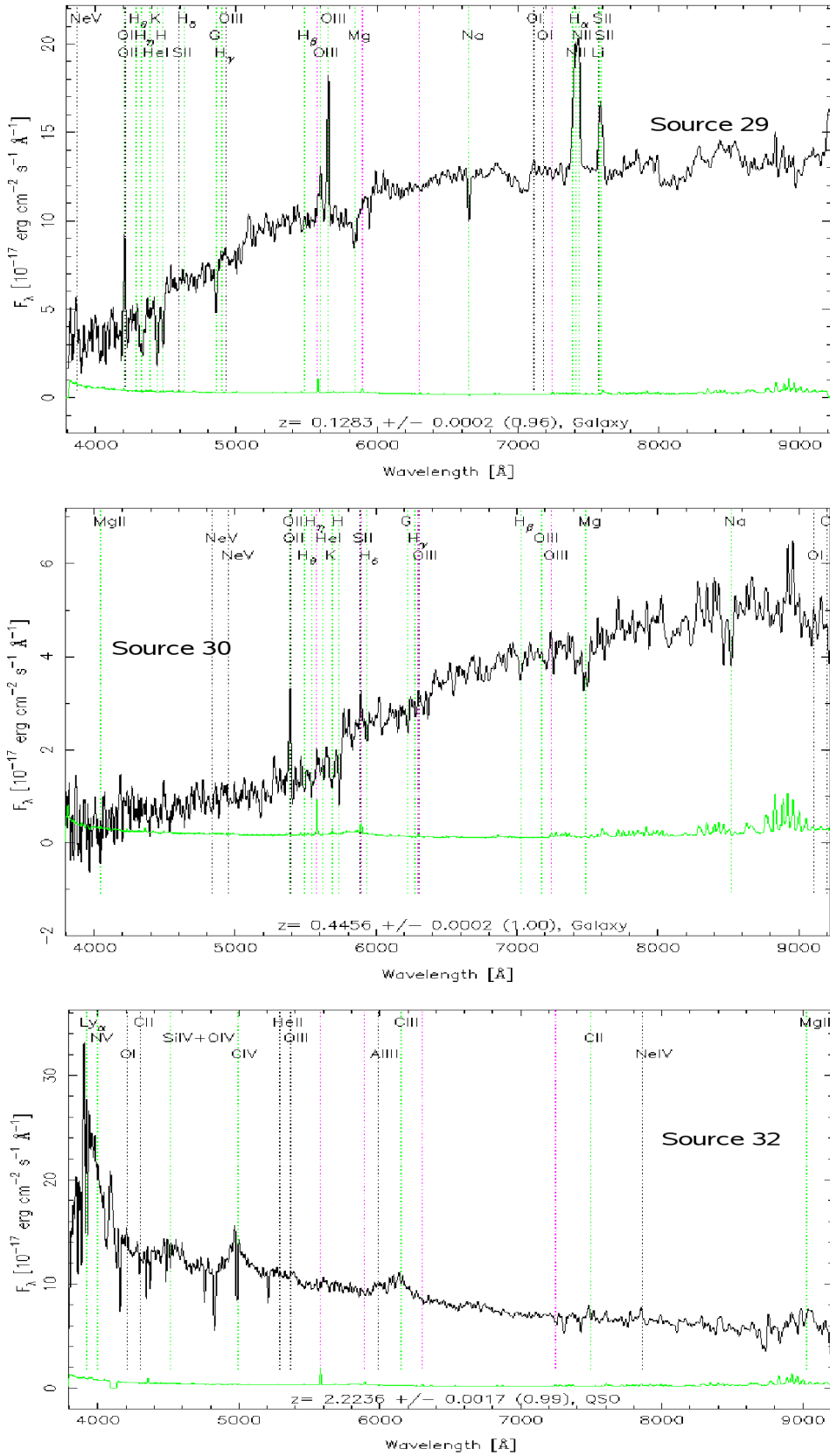


Figure 19 – continued

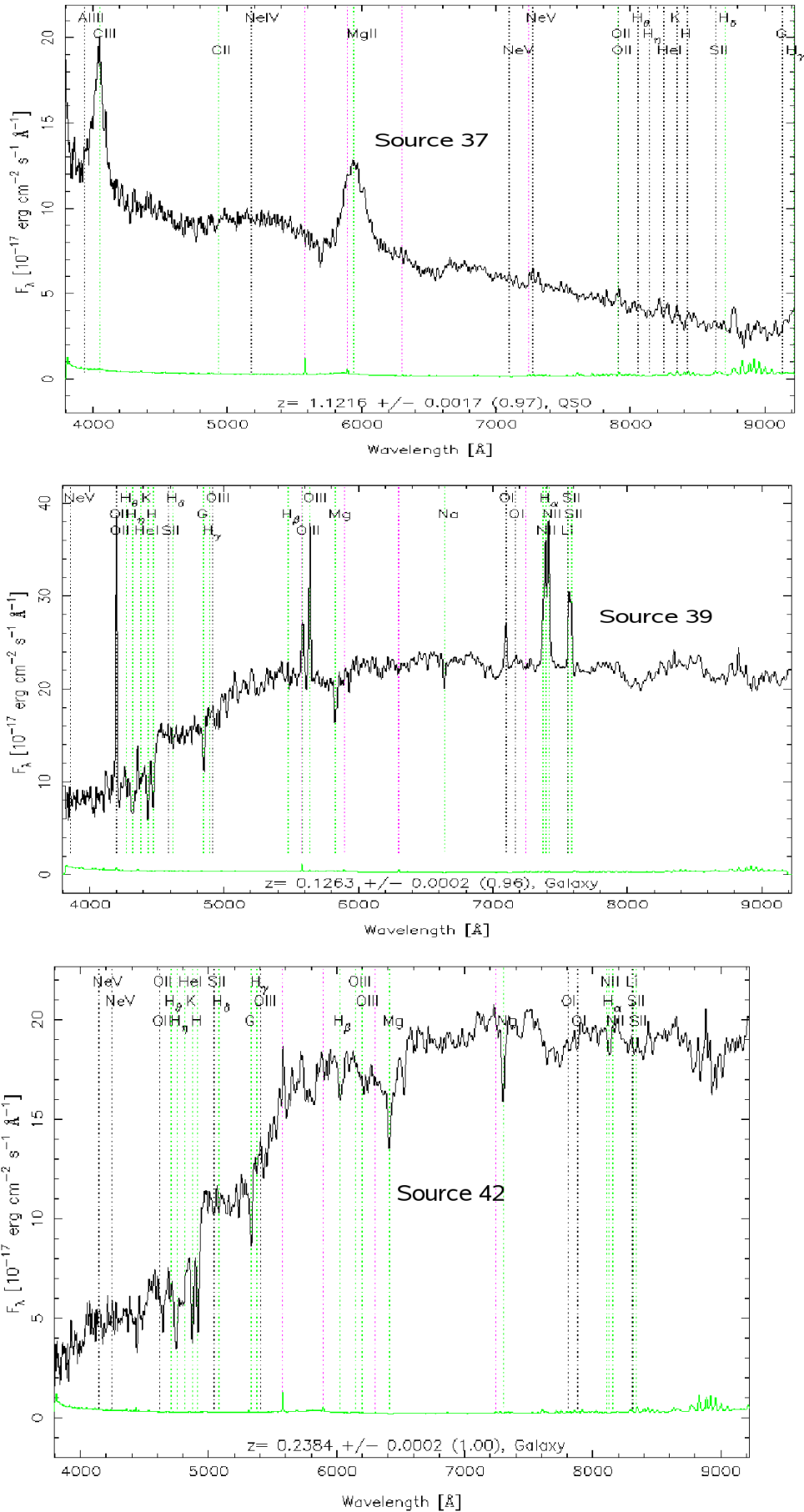


Figure 19 – continued

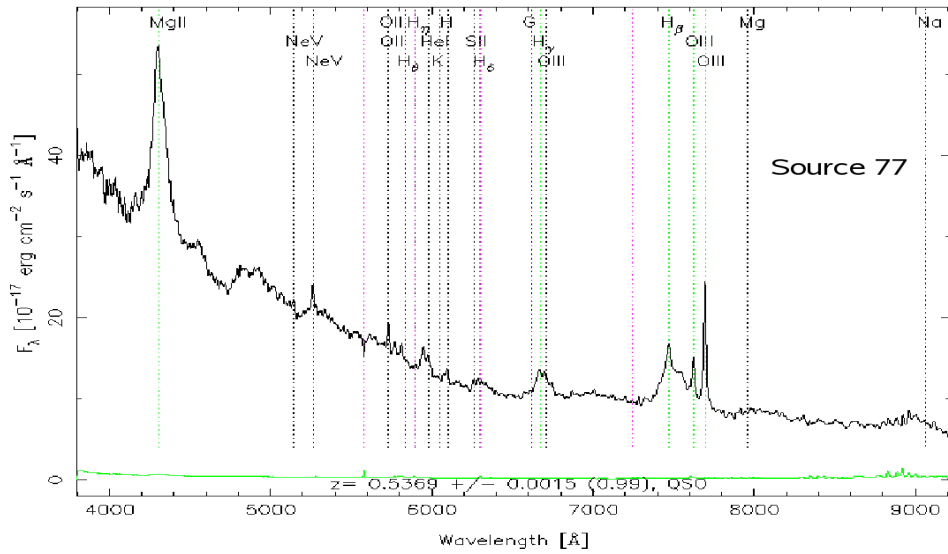
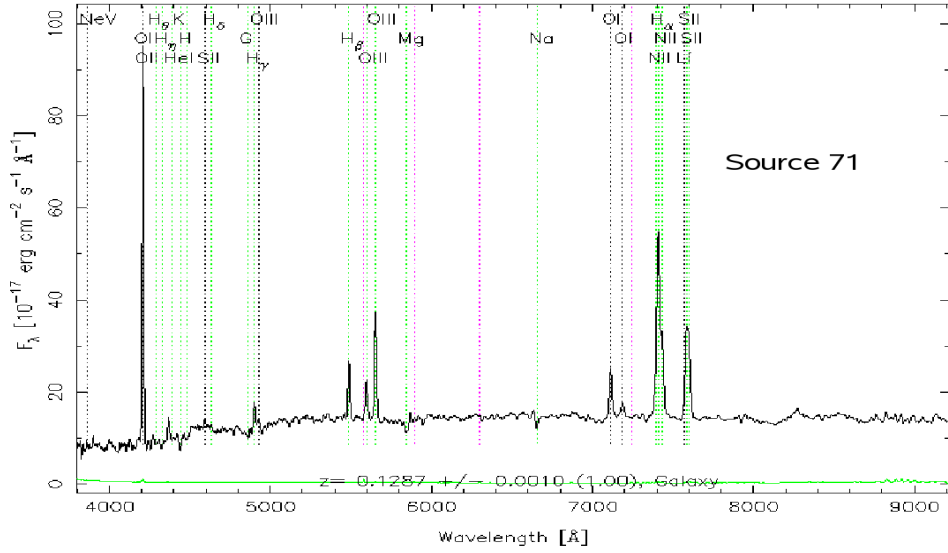
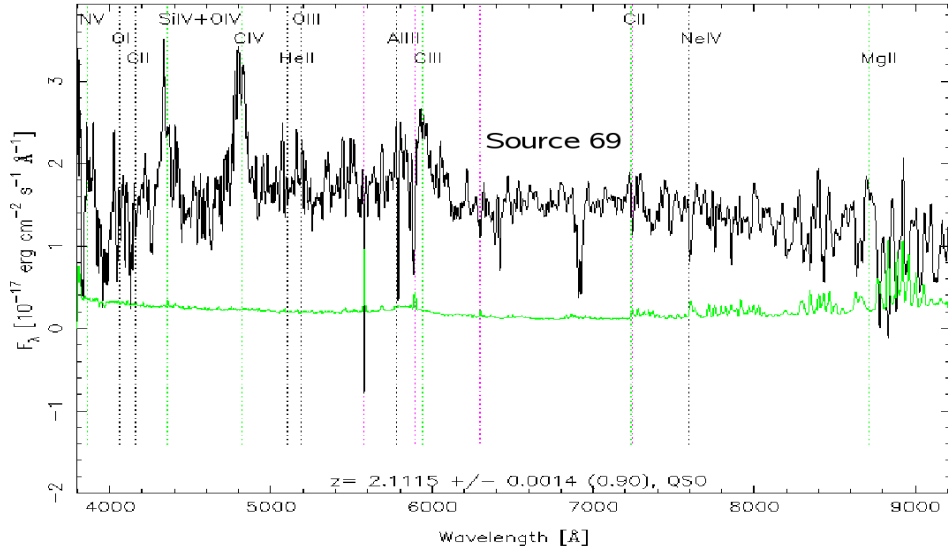


Figure 19 – continued

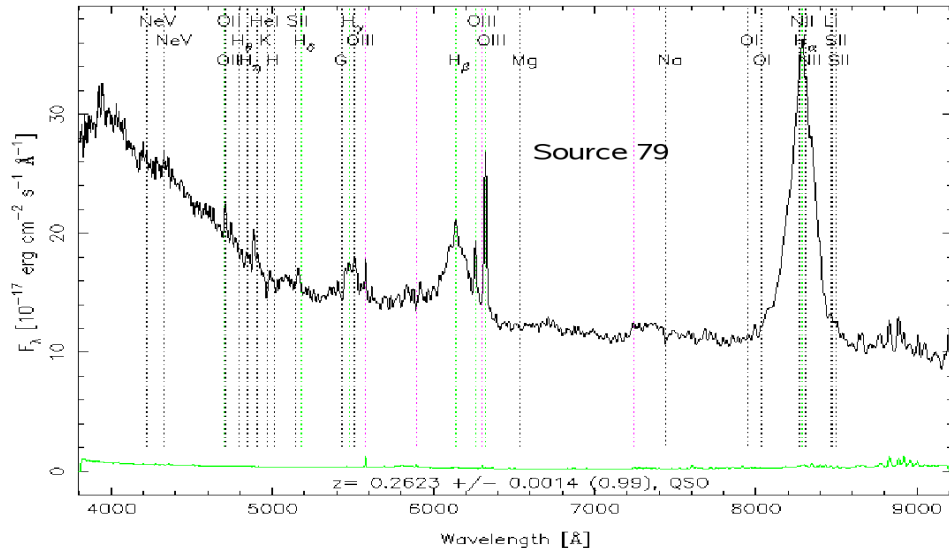


Figure 19 – continued